Multiple-instance superparameterization, part 2: the effects of stochastic convection on the simulated climate

JAMES | Journal of Advances in Modeling Earth Systems

RESEARCH ARTICLE
10.1029/2019MS001611

This article is a companion to Jones et al. (2019), https://doi.org/10.1029/2019MS001610.

Key Points:
- Multiple-instance superparameterization is presented as a more deterministic analogue to standard superparameterization
- Several measures verify the increased level of determinism resulting from the new parameterization
- The parameterization formulation yields a similar model climate with a slightly degraded MJO

Supporting Information:
- Supporting Information S1

Correspondence to:
T. R. Jones,
t.r.jones@reading.ac.uk

Citation:
Jones, T. R., Randall, D. A., & Branson, M. D. (2019). Multiple-instance superparameterization: 2. The effects of stochastic convection on the simulated climate. *Journal of Advances in Modeling Earth Systems*, *11*, 3521–3544. https://doi.org/10.1029/2019MS001611

Received 9 JAN 2019
Accepted 5 SEP 2019
Accepted article online 10 SEP 2019
Published online 15 NOV 2019

Multiple-Instance Superparameterization: 2. The Effects of Stochastic Convection on the Simulated Climate

Todd R. Jones[1], **David A. Randall**[2], **and Mark D. Branson**[2]

[1]Department of Meteorology, University of Reading, Reading, UK, [2]Department of Atmospheric Science, Colorado State University, Fort Collins, CO, USA

Abstract The cloud-permitting model (CPM) of the superparameterized Community Atmosphere Model (SP-CAM) is a stochastic parameterization. As reported in a companion paper, we have created a variant of SP-CAM, called MP-CAM, that uses the averaged feedback of 10 independent two-dimensional CPMs in each global model column, in place of the single CPM of SP-CAM. This ensemble-averaged feedback is interpreted as an approximation to the feedback from a deterministic parameterization. We present evidence that the multiple-instance superparameterization of MP-CAM is indeed more deterministic than SP-CAM. The climates of the SP and MP configurations are compared, giving particular attention to extreme precipitation events and convectively coupled large-scale tropical weather systems, such as the Madden-Julian Oscillation. A number of small but significant changes in the mean state climate are uncovered, and the deterministic parameterization slightly degrades the Madden-Julian Oscillation simulation.

1. Introduction

Realistic simulations of precipitation, including probability, timing, location, type, and amount, are of great practical importance. Unfortunately, precipitation is one of the most difficult atmospheric phenomena to simulate well—especially its variability and its extremes. Extreme precipitation events can have dramatic consequences in the form of floods and droughts, which are among the most damaging weather-related natural disasters, both in terms of lives lost and economic impact (National Centers for Environmental Information, 2019; Smith & Katz, 2013).

When evaluating weather forecasts, decision makers must consider not just the predicted variables of interest (e.g., precipitation amount) but also their uncertainty. Forecast uncertainty can be quantified using ensemble forecasts, which produce probabilities of occurrence based on multiple, slightly different simulations that reveal the range of potential solutions (Bauer et al., 2015; Berner et al., 2015; Epstein, 1969; Harnisch & Keil, 2015; Leith, 1974; Molteni et al., 1996; Mureau et al., 1993; Palmer, 2000; Palmer et al., 1993; Toth & Kalnay, 1993, 1997; Tracton & Kalnay, 1993).

Poor forecasts often result from rapid error growth that starts on the smallest scales included in the model (Molteni et al., 1996; Palmer, 2000; Walser et al., 2004). An important additional source of uncertainty is in the representation of moist convective processes *below* the grid scale (Flato et al., 2013). The spatial resolution of most atmospheric global circulation models (GCMs) is too coarse to allow the explicit representation of physical processes from approximately the mesoscale on down. Such processes have to be parameterized. The parameterization of cloud processes, especially moist convection, is a perennially active area of research (Jakob, 2014; Stevens & Bony, 2013). Despite 40 years of improvements, significant and persistent deficiencies remain in the treatment of clouds, resulting in errors in the simulations of weather and climate (Kim et al., 2009; Lin et al., 2006; Randall et al., 2003; Slingo et al., 1996, 2005).

With coarse grids, parameterizations are required to provide only the "expected values" of the convective tendencies, but with finer grids they should allow simulations of individual realizations of convective systems. Parameterizations that are designed to give expected values can be called deterministic. They cannot represent the "stochastic" variability of convection that arises from the intrinsically uncertain nature of small-scale motions, through sensitive dependence on initial conditions (Arakawa, 2004; Jones & Randall, 2011; Hohenegger & Schär, 2007; Lorenz, 1969; Randall & Ding, 1997; Randall et al., 1994; Shutts & Palmer, 2007; Xu et al., 1992; Xu & Randall, 1998).

It has been argued that the chaotic behavior of real cloud systems needs to be included in convection parameterizations designed for use in lower-resolution models (e.g., Berner et al., 2012; Hohenegger & Schär, 2007).

For example, Neelin et al. (2008) suggested that stochastic parameterizations are needed for a realistic simulation of the Madden-Julian Oscillation (MJO). The use of stochastic physics has been shown to increase the "spread" of forecast ensembles (Berner et al., 2012; Buizza et al., 1999) and can enable noise-induced transitions between weather regimes (Hasselmann, 1976). Stochastic physics has been shown to produce forecast improvements and reduce some systematic biases (e.g., Bowler et al., 2009; Charron et al., 2010; Davini et al., 2017; Strømmen et al., 2018; Watson et al., 2017). Research on stochastic parameterizations has recently been reviewed by Berner et al. (2017).

In this paper, we focus on a particular type of stochastic parameterization: superparameterization (hereafter, SP), in which the conventional parameterizations are replaced by a two-dimensional cloud-permitting model or CPM (Grabowski, 2001; Grabowski & Smolarkiewicz, 1999; Khairoutdinov & Randall, 2001; Khairoutdinov et al., 2005), with a horizontal grid spacing on the order of a few kilometers and periodic lateral boundary conditions. One copy of the CPM runs continuously and independently in each GCM column. Microphysics, radiation, and turbulence must still be parameterized, but the parameterizations are implemented on the CPM's fine grid. An SP simulates individual realizations of cloud systems, rather than expected values. Because small-scale noise arises naturally from the CPM's sensitive dependence on initial conditions, an SP behaves stochastically without the need for a random number generator.

A number of studies (DeMott et al., 2007; Kooperman et al., 2016; Li et al., 2012; Rosa & Collins, 2013) have demonstrated the ability of SP to realistically simulate precipitation extremes. Li et al. (2012) demonstrated SP's skill in simulating high-percentile precipitation rates over the continental United States. Khairoutdinov and Zhou (2015) present results of a similar comparison using global and tropical data. Subramanian and Palmer (2017) examined both stochastic and SP methods in simulations using the European Centre for Medium-Range Weather Forecasts Integrated Forecasting System. They reported that, relative to stochastic ensemble forecasts, SP ensemble forecasts give more realistic simulations of tropical waves and intraseasonal variability and also improvements in the modeling of uncertainty in tropical convection, MJO initiation, and tropical cyclones. The extent to which the stochastic nature of SP is responsible for those improvements remains an open question.

As discussed in a companion paper (Jones et al., 2019), we have developed a variation on the SP concept in which the GCM feels the ensemble-averaged feedback from multiple realizations of the cloud field as simulated by multiple CPMs. We call this approach "multiple-instance superparameterization," and the global atmospheric model is called MP-Community Atmosphere Model (CAM). The MP approach effectively turns the nondeterministic SP into a deterministic parameterization by "brute force" averaging over the ensemble of heating and drying realizations simulated by the individual CPMs. This averaged feedback is an approximation to an expected value. Because of the averaging over realizations, the extreme values of the SP heating and drying rates produced in individual CPM simulations are smoothed out.

This paper compares the atmospheric circulations simulated by SP-CAM and MP-CAM, both run with prescribed climatological sea surface temperatures. How might the simulated climate be affected by the implementation of the MP configuration? Precipitation extremes (including the occurrence of zero precipitation) would surely be reduced, but would the model lose fidelity in large-scale features, like the MJO, whose realistic simulation has been hypothesized to depend on the stochasticity of moist convection? Comparison of simulations with SP-CAM and MP-CAM can show to what extent and in what ways nondeterministic effects are important (Bechtold et al., 2013; Donner & Phillips, 2003; Zhang, 2002). These issues are the focus of this paper.

Following a brief description of the models and how they are configured (section 2), we investigate to what degree MP-CAM behaves like a more deterministic version of SP-CAM (section 3). We then present an analysis that reveals some differences in the climates simulated by the two models (section 4), including differences in the simulated intraseasonal variability (section 5). Conclusions are given in section 6.

2. Methods and Data

2.1. Models

The particular configurations of SP-CAM and MP-CAM used in this study are described by Jones et al. (2019). Briefly, our simulations use the base source code of the Community Earth System Model 1.1.1,

which includes Version 5.2 of the CAM (Neale et al., 2012), run with the finite-volume dynamical core that solves the hydrostatic equations of motion on a 1.9° × 2.5° latitude-longitude grid. The model uses 26 levels with a terrain-following hybrid σ-p coordinate. Radiation calculations are performed every 15 simulated minutes using CAM radiation (Neale et al., 2010). MP-CAM uses 10 CPMs that are run in each GCM grid column, each configured exactly as in SP-CAM. Each CPM is initialized with a unique set of weak random thermal perturbations, so that the CPMs start out with slightly different initial conditions. Additionally, the *cam4* physical parameterization package (Neale et al., 2010) is used in a noninteractive, diagnostic fashion; this package includes parameterization of deep convection via the Zhang-McFarlane convection scheme (Zhang & McFarlane, 1995), modified to include the plume-diluting effects of entrainment (Neale et al., 2008) and convective momentum transport (Gregory et al., 1997; Richter & Rasch, 2008), shallow convection following Hack (1994), and stratiform cloudiness following Sundqvist (1988), Zhang et al. (2003), and Rasch and Kristjánsson (1998).

All CPMs in a given GCM grid column see exactly the same large-scale weather. Because of their slightly different initial conditions, the 10 CPMs will produce different cloud fields and tendencies. The GCM sees only the ensemble mean heating and drying rates, which should be temporally smoother than heating and drying rates from the single CPM used in SP-CAM. We expect that with this "expected feedback," the parameterized convective forcing will be more deterministic than the feedback in SP-CAM, with its single CPM in each GCM grid column.

To compare the climates produced by SP-CAM and MP-CAM, multidecadal simulations have been performed with each model. Using NCAR's Yellowstone supercomputer, SP-CAM was run for 30 years, and MP-CAM was run for just over 23 years. Output was recorded in the form of monthly and daily time averages for both models, but evolving needs and demands yielded a data set with irregular availabilities for some model diagnostics. Higher-frequency output was also created for January and July subsets of the MP-CAM simulation. Three-hourly averaged data were created for July of year 7 and January of year 8 as well as for August of year 20 through the end of the simulation. Records were saved every 15 min (every GCM time step (ETS), with averages over only the CPM subcycle, hereafter ETS data) for individual sample days from January to July. ETS data were also created for SP-CAM for a single January day. For more complete documentation of the data sets, see Jones (2017).

We also created a 30-year simulation with the standard CAM, using the *cam4* physical parameterization package. This standard CAM simulation is consistent with the SP-CAM and MP-CAM in terms of grid and initialization. Most of the GCM-level model diagnostics recorded in the SP and MP simulations were also saved in this run as monthly and daily averages for the full simulation period. This standard CAM simulation allows us to compare SP and MP results with those produced with a conventional parameterization.

2.2. Observational Data

The simulated daily mean outgoing longwave radiation (OLR) data are compared with the daily mean National Oceanic and Atmospheric Administration (NOAA) interpolated OLR data set (Liebmann & Smith, 1996). The NOAA OLR data set is interpolated in time and space from twice daily values and averaged to once daily with a latitude-longitude resolution of 2.5° × 2.5°. We use the 30-year record from 1 January 1980 to 31 December 2009.

Two observational precipitation data sets are used for comparison to the simulated data. Both were obtained from the National Center for Atmospheric Research's Climate and Global Dynamics Laboratory and are available online (ftp://ftp.cgd.ucar.edu/archive/PRECIP). The first is a global product from the Global Precipitation Climatology Project (GPCP, version 1.2), known as the GPCP One-Degree Daily Precipitation Data Set (Huffman et al., 2001). As its name suggests, the data are daily estimates of precipitation presented on a global 1° × 1° latitude-longitude grid, representing a complex combination of infrared and microwave satellite-based measurements and surface rain gauge measurements that were originally made at higher temporal resolution. The available data span 6,878 days, from October 1996 to July 2015.

The second observational precipitation data set comes from the Tropical Rainfall Measuring Mission (TRMM), which provides 3-hourly precipitation rate estimates on a 0.25° × 0.25° latitude-longitude grid with spatial coverage in the latitude band from 50°S to 50°N. The TRMM data used here are derived from a set of satellite-based microwave; visible, infrared, and radar instruments; and rain gauges. More specifically, this is

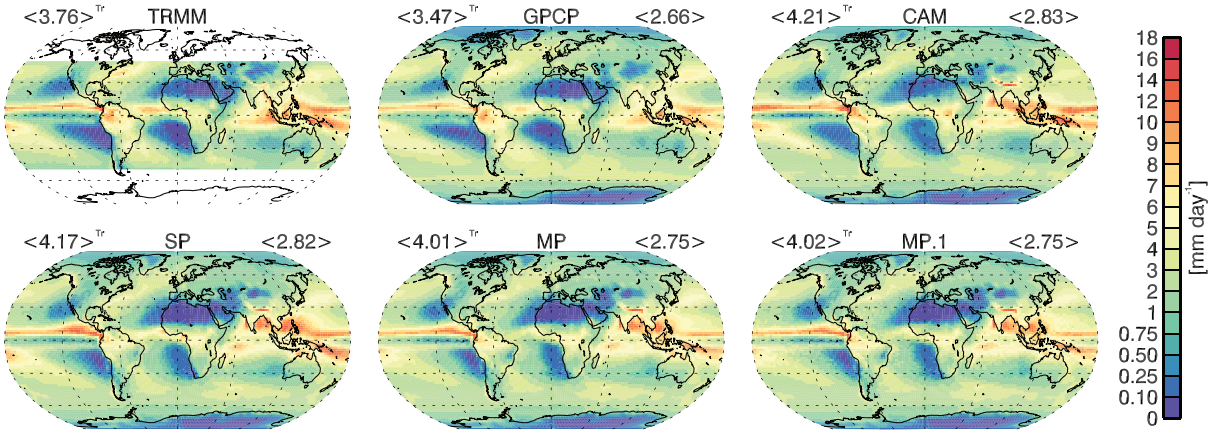

Figure 1. Annual mean precipitation rate for the full indicated observational and simulated data sets. MP.1 is the first CPM member of the MP simulation. <*x*> denote spatial averages: the upper left value, annotated with superscript Tr, is an average from 20°S to 20°N, representing tropical values, and the upper right value is the global mean. TRMM = Tropical Rainfall Measuring Mission; GPCP = Global Precipitation Climatology Project; CAM = Community Atmosphere Model; SP = superparameterized; MP = multiple-instance superparameterization.

known as the TRMM Multisatellite Precipitation Analysis product 3B42 version 7, compiled by Huffman et al. (2007). The TRMM data obtained from Climate and Global Dynamics were already averaged to a daily precipitation estimate, spanning 5,844 days, from January 1998 to December 2013. To facilitate comparison to the model output, both observational precipitation data sets were regridded to the CAM's grid, using a conservative interpolation (Jones, 1999) that preserves the spatial integral of the data. The two precipitation data sets have differences in spatial distribution, frequency distribution, and temporal variability (Gehne et al., 2016; Kooperman et al., 2016).

3. Is MP-CAM Really More Deterministic Than SP-CAM?

3.1. Analysis of Standard Deviations

As mentioned in section 2 one goal in creating MP-CAM was to create a deterministic convection parameterization. As more CPMs are used in each GCM grid column, the temporal variance of the ensemble-averaged data should decrease. For the case of 10 estimates of a completely random system, we would expect to see the standard deviation fall off by $\sqrt{10}\approx 3.16$. For partially random data, the reduction in standard deviation due to averaging will be less than $\sqrt{n}$. Further discussion is given by Jones (2017).

We can apply this concept to the set of simulations in this study by considering the time series of precipitation as simulated by SP as the representative sample and that simulated by MP as the averaged data set.

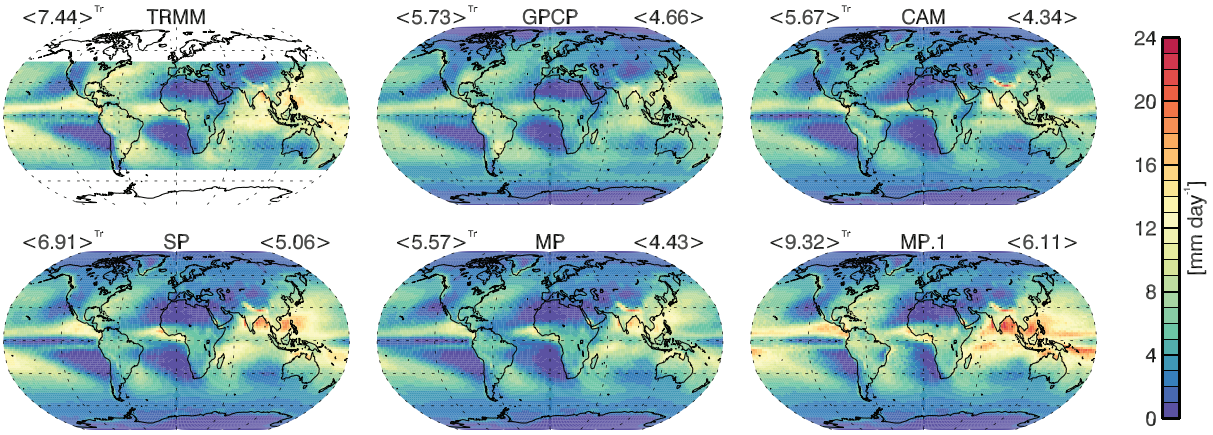

Figure 2. As in Figure 1 but for the temporal standard deviation of the daily mean precipitation rate, with the annual cycle retained.

Table 1
Global and Tropical (^{Tr}) RMSE and Spatial Correlation (r) of the Annual Mean Precipitation Spatial Pattern for the Model Simulations Relative to GPCP or TRMM

	GPCP				TRMM	
Model	RMSE	r	RMSE^{Tr}	r^{Tr}	RMSE^{Tr}	r^{Tr}
CAM	1.126	0.884	1.593	0.869	1.499	0.872
SP	1.219	0.871	1.821	0.816	1.701	0.832
MP	1.144	0.869	1.641	0.812	1.625	0.823
MP.1	1.146	0.868	1.643	0.811	1.631	0.822

Note. RMSE = Root-Mean-Square Error; GPCP = Global Precipitation Climatology Project; TRMM = Tropical Rainfall Measuring Mission; CAM = Community Atmosphere Model; SP = superparameterized; MP = multiple-instance superparameterization.

Figures 1 and 2 show maps of the temporal mean and temporal standard deviation of precipitation from TRMM, GPCP, CAM, SP, MP, and MP.1; here MP.1 is the first CPM member of the MP simulation. A comparison of the simulations to observations is summarized in Table 1. In this case, the temporal standard deviation is based on daily mean data, retaining the annual cycle.

As reported in previous studies (e.g., Kooperman et al., 2016), spatial means from each of the simulations are greater than observed, though the MP results shown in Figure 1 are closest to GPCP and TRMM. The largest differences are found in the tropics, particularly over wet-biased oceans just off the equator. As discussed by Randall et al. (2016), this wet bias largely disappears when SP-CAM is coupled with an ocean model. The simulations produce less precipitation than observed over some tropical land areas, notably South America and the Maritime Continent. Table 1 gives the root-mean-square error and spatial correlations. Lower root-mean-square error and higher spatial correlations both globally and in the tropics show that CAM best captures the spatial distribution. This is largely due to better representations of precipitation over South America, Southeast Asia, and the Maritime Continent. On the other hand, CAM performs less well along the Intertropical Convergence Zone (ITCZ) in the Pacific. A strong wet bias occurs over the Himalayas in each model; this is probably a topographic effect.

For the purposes of characterizing MP's level of determinism, we are interested in the temporal standard deviation information shown in Figure 2. The standard deviation tends to be roughly proportional to the mean precipitation, with spatial biases in standard deviation similarly following those in mean precipitation. Comparing spatial averages, we see that TRMM, with greater variability than GPCP, is the closest match to SP, whereas standard deviations are mostly lower than SP in GPCP, CAM, and MP. Also notable are the overall higher standard deviations in MP.1. This is the first indication that a single CPM member in MP is not precisely equivalent to the one operating in SP; more discussion is given later.

Overall, the temporal standard deviation decreases from SP to MP, especially in the tropics. This decrease indicates that the MP configuration does produce a more deterministic precipitation time series, as expected (Figure 3).

Most places have the standard deviation fall-off ratio, σ_{SP}/σ_{MP}, greater than 1. The global average, 1.12, is exceeded on 35% of the globe. Areas between 1.5 and 3.25 (yellow to orange colors, indicating significantly greater determinism in MP) account for just over 6% of the globe. Figure 4 shows precipitation rate

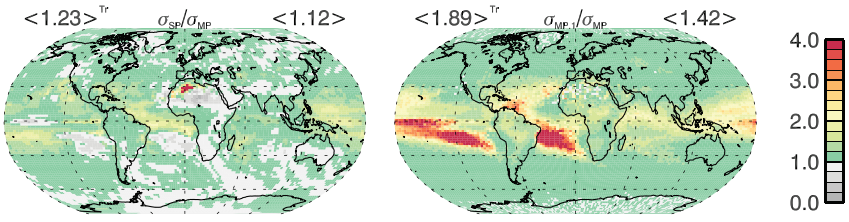

Figure 3. Precipitation rate temporal standard deviation (as in Figure 2) fall-off ratio for σ_{SP}/σ_{MP} (left) and $\sigma_{MP.1}/\sigma_{MP}$ (right). <*x*> denote spatial averages: the upper left value, annotated with superscript Tr, is an average from 20°S to 20°N, representing tropical values, and the upper right value is the global mean.

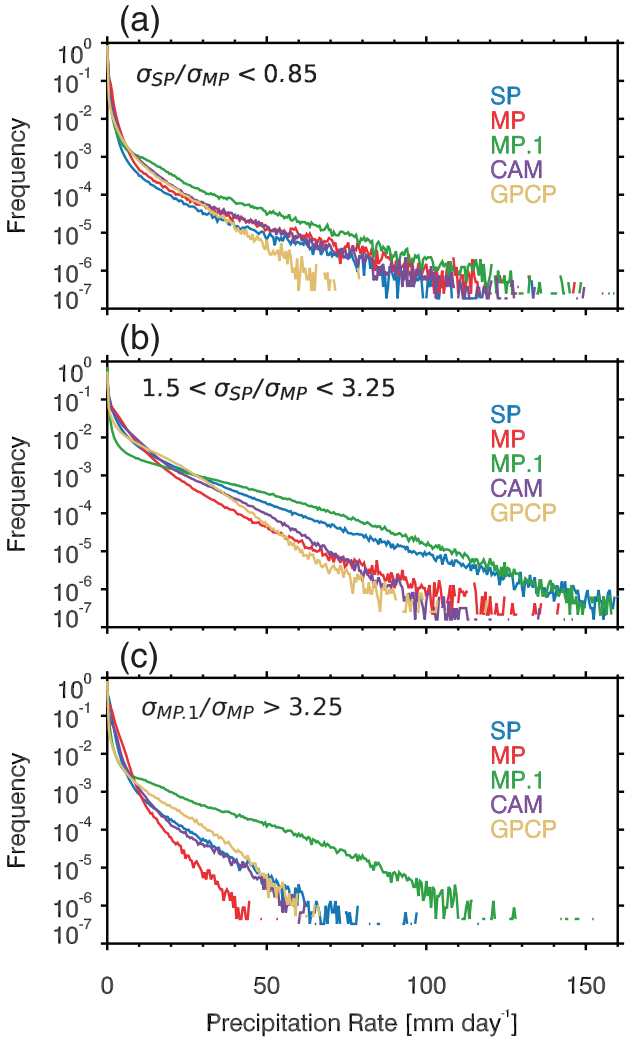

Figure 4. Precipitation rate probability density function for points where σ_{SP}/σ_{MP} (Figure 3) is (a) less than 0.85 and (b) between 1.5 and 3.25, and (c) where $\sigma_{MP.1}/\sigma_{MP}$ is greater than 3.25. MP = multiple-instance superparameterization; CAM = Community Atmosphere Model; GPCP = Global Precipitation Climatology Project; SP = superparameterized.

probability density functions (PDFs) for regions of interest in Figure 3. In these moderate fall-off ratio locations, the MP.1 precipitation distribution is much closer to that of SP for larger precipitation rates (Figure 4b), and the averaging in MP results in an MP distribution quite different from that of MP.1 and closer to that from CAM. There are a few regions in which the ratio is less than one (Figure 3a), indicating greater variability in MP. This is surprising because averaging of similar data sets should almost exclusively give a ratio greater than 1. Where the standard deviation fall-off ratios are less than 0.85 (5% of the globe), the averaging of the MP CPMs yields a weak reduction in higher precipitation rates (Figure 4, left panel). Instead, the change puts the PDF of MP more in line with SP and CAM. The weak change in PDFs (MP.1 to MP) means that more of the CPMs agree about the precipitation rate more often, indicating good predictability in these areas. (See Jones et al., 2019, for additional discussion of precipitation predictability in MP-CAM.) MP is also a closer match to CAM for precipitation less than 5 mm/day, except for very low rates, which are less frequent in MP due to the averaging.

The right panel of Figure 3 confirms that MP.1 behaves as a sample data set, and MP behaves as mean of sample data sets. In the global mean, the standard deviation fall-off ratio is 1.42, indicative of stronger randomness reduction. A skewing factor in the global mean value, though, lies in points where the standard deviation fall-off ratio is even greater than value that would be obtained if analyzing the mean of ten purely random data sets against one of its members, namely $\sqrt{10}$. These deep red colors over the southern oceans

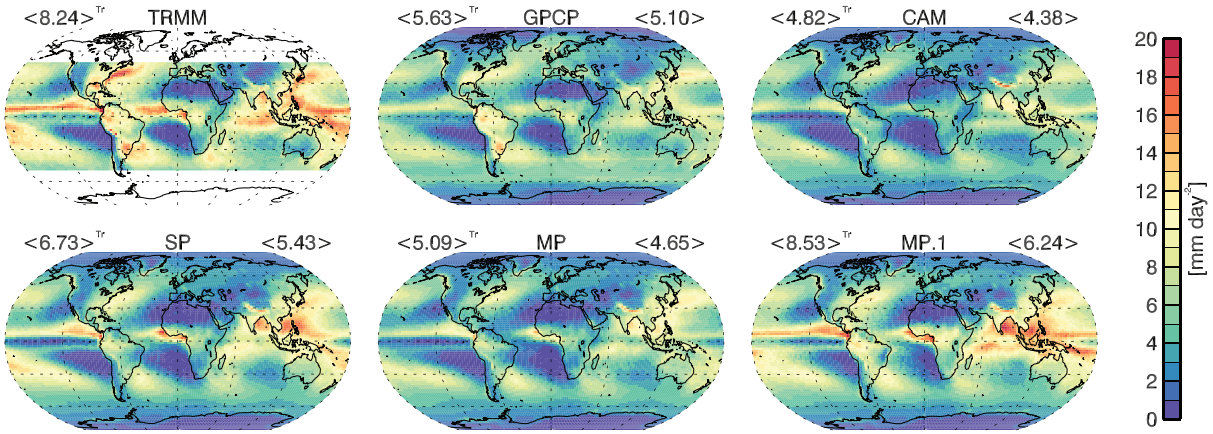

Figure 5. As in Figure 1 but for the temporal jaggedness for daily precipitation rate.

account for slightly more than 3% of the global surface area, and are characterized by MP.1 precipitation rates less than 0.5 mm/day. When averaged, these points more frequently see values up to 3–4 mm/day due to wet outliers, resulting in many fewer dry days at these points in MP relative to MP.1. The process of averaging increases typically low values toward the large outliers. This is another indication that MP.1 is not doing the same thing as SP-CPM. MP.1 produces much more frequent and greater extremes than SP, CAM, and GPCP at these points, mostly because of its feedback to the parent GCM. In some cases, MP's CPM ensemble includes a large majority of members with very low precipitation rates and only one or two with very high precipitation rates. Some reasons for this are discussed by Jones et al. (2019).

3.2. Analysis Based on the Coefficient of Variation

As discussed in Jones et al. (2019), the coefficient of variation (COV, sometimes written as CV or CoV) is defined as the standard deviation divided by the mean. It is often used as a normalized indicator of noise in a data set that allows for comparison between data sets of characteristically disparate magnitudes, such as climatologically wet and dry regions. A COV less than one is consistent with relatively deterministic and predictable precipitation, while large COVs are consistent with chaotic, unpredictable precipitation. Here, "unpredictable" is relative to the scale of the mean.

The COVs for precipitation and OLR exhibit patterns similar to those seen in standard deviation fall-off ratio (not shown). CAM gives the lowest values, indicating the greatest determinism; SP is characterized by greatest stochasticity. Determinism increases from SP to MP for precipitation but not for OLR. More specifically, globally averaged precipitation COV values of 1.86, 2.26, 2.49, and 2.96 are reported for CAM, MP-CAM, SP-CAM, and MP.1, respectively. As far as the COV measures are concerned, precipitation changes suggest that MP is more closely constrained to some expected value, while a shift in cloudiness causes OLR to be more widely varying across much of the tropics. The same analysis carried out at 3-hourly temporal resolution also gives qualitatively similar results.

3.3. Additional Measures of Determinism

While the standard deviation fall-off ratio and the COV changes provide guidance as to the change in determinism, they do not take into account the temporal sequence of the data. For instance, sets $S_1 = \{50, 50, 25, 25, 0, 0, 0, 0\}$ and $S_2 = \{50, 0, 50, 0, 25, 0, 25, 0\}$ have the same mean and standard deviation, but in terms of temporal persistence, the first sequence seems more predictable. A measure that accounts for this is the *e*-folding time of the autocorrelation function. By this measure, using both daily and 3-hourly data, the tropically averaged *e*-folding times are 4.5 days for CAM, 4 days for MP, 3 days for SP, and 2.75 days for MP.1. Similar results are obtained using the OLR.

The *e*-folding time is helpful but can be problematic. As an example, consider again the sets S_1 and S_2, which were discussed above. Autocorrelations can be large at large lags, despite drastic fluctuations from one time to the next. To deal with this issue, we examine the "temporal jaggedness" of the data via a measure that combines elements of the temporal derivative and the root-mean-square difference, given by

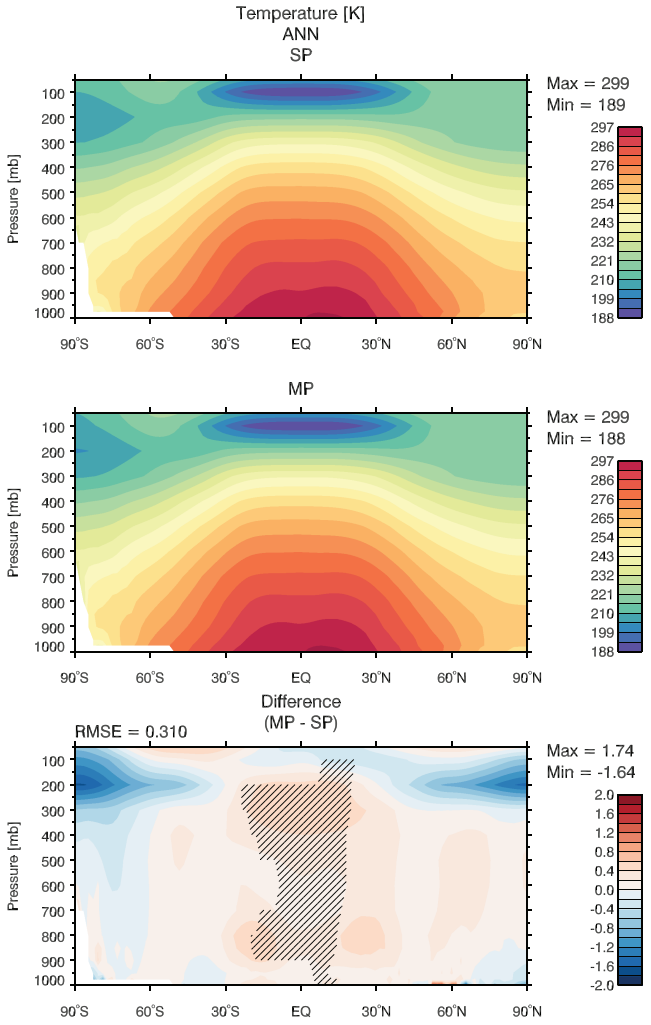

Figure 6. Annual mean, zonal mean profile of absolute temperature for SP (top), MP (middle), and the MP-SP difference (bottom). Diagonal black lines indicate areas of statistically significant differences as described in the text. SP = superparameterized; MP = multiple-instance superparameterization; RMSE = root-mean-square error; ANN = annual mean.

$$J = \sqrt{\frac{\sum_{n=1}^{N} \left(\frac{x_{n+1} - x_n}{\delta t}\right)^2}{N-1}}. \quad (1)$$

Here N is the number of values (x) in the sequence, indexed by n. This measure is not normalized, meaning that strong absolute shifts are given emphasis. The temporal jaggedness of the daily mean precipitation rate is shown in Figure 5. When normalized by mean values of the temporal derivative, these plots almost exclusively highlight areas of climatologically low precipitation with high jaggedness (not shown). In Figure 5, CAM and MP show smaller temporal jaggedness, indicating a smoother field and greater predictability. Areas with large jaggedness include the midlatitude storm tracks and the ITCZ. In a similar analysis using 3-hourly data (not shown), strong continental maxima of temporal jaggedness are associated with diurnal convection. Applying equation (1), but with N as the number of points in the vertical and the derivative with respect to pressure, Figure S1 (supporting information) shows the reduction in the vertical variation of temperature and moisture tendencies from SP's single CPM to MP's CPM ensemble average for one simulated month. These smoother profiles are fed back to the MP GCM.

A potentially more rigorous characterization of determinism can be provided by measures such as fractal dimension and Lyapunov exponents (Grassberger & Procaccia, 1983; Takens, 1981). These methods of

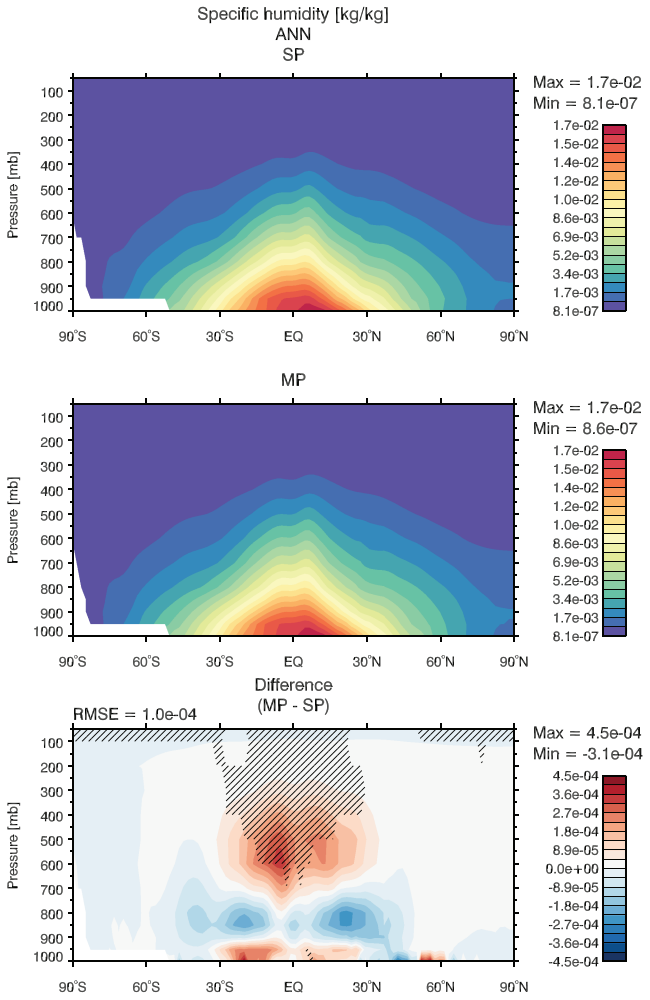

Figure 7. As in Figure 6 but for specific humidity.

chaotic time series analysis have been used to measure predictability in a variety of geophysical parameters (e.g., Chen et al., 2006; Ding et al., 2008; Liu et al., 2016; Millán et al., 2011, 2009; Sivakumar, 2001, 2004; Zeng et al., 1992). Analysis of our precipitation and OLR data (supporting information Text S1 and Figure S2) provides some support to the characterization of MP as more deterministic than SP. However, analysis of the precipitation data is inconclusive and that for OLR is not statistically significant.

Based on the combined results of the standard deviation fall-off, COV, *e*-folding times, temporal jaggedness, and, to a lesser extent, chaotic time series analysis, we conclude that the daily mean precipitation rate is in fact more deterministic in MP than in SP, as intended.

4. Simulated Annual Means

4.1. Differences in the Simulated Mean States

For each of many variables, defined at selected pressure levels, the spatially varying differences between MP and SP were computed annually and seasonally. The root-mean-square differences of the time-averaged spatial patterns, normalized by the range of their values in SP, were used to identify large differences. Significant differences (at the 95% confidence level) were calculated based on means testing using a two-sided Student's *t* distribution at each location, with the conservative assumption of one independent sample per season.

In addition, time series of various global means were subjected to a wider range of tests in order to identify significant differences. The most stringent test used Student's *t* distribution with the assumption of one

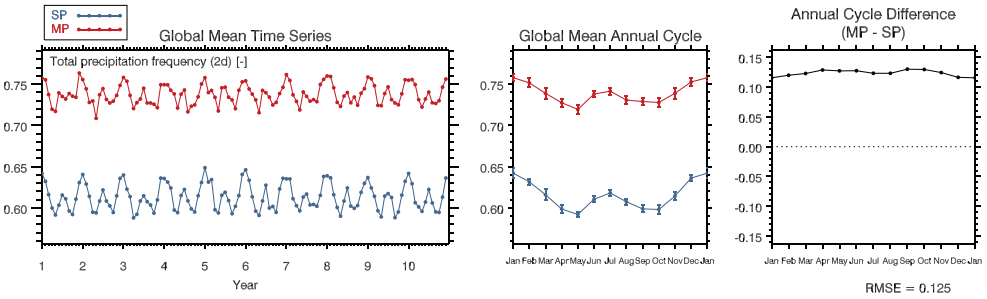

Figure 8. Global mean statistics of precipitation frequency for SP-CAM (blue) and MP-CAM (red): (left) a 10-year time series, (middle) their mean annual cycles, and (right) the difference in their annual cycles. SP = superparameterized; MP = multiple-instance superparameterization; RMSE = Root-Mean-Square Error.

independent sample per year. A less stringent, but probably more accurate, test estimates the effective number of independent samples following the method of Bretherton et al. (1999), which accounts for the effects of persistence.

Significance tests of differences in the mean annual cycle and the correlations of the global mean time series for each variable at several pressure levels and their annual cycles were performed to look for potential phase shifts in the seasonality of the global means. The time series were also compared using the signs test for

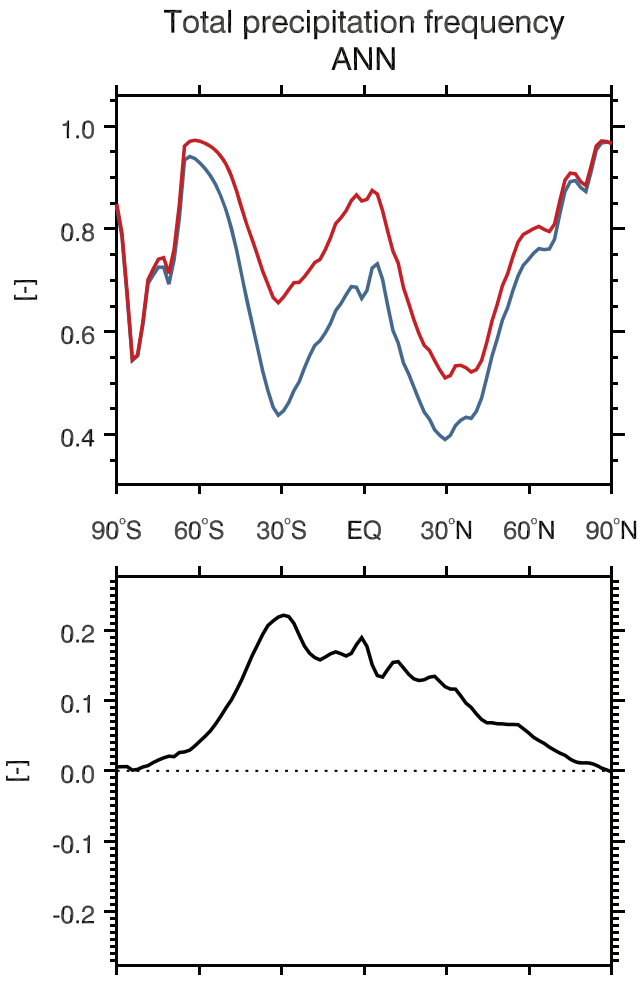

Figure 9. Zonal mean of the annual mean precipitation frequency for (top) superparameterized (blue) and multiple-instance superparameterization (red) and (bottom) their difference. ANN = annual mean.

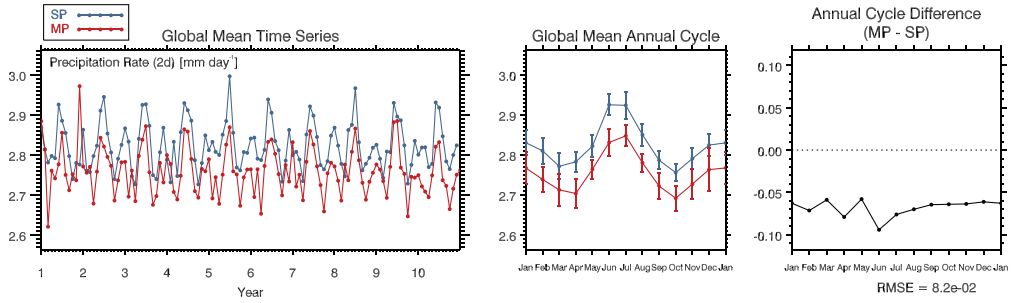

Figure 10. As in Figure 8 but for the precipitation rate.

nonparametric data that do not conform to a normal distribution. Identification of features exhibiting greatest differences was aided by computation of the root-mean-square difference normalized by the range of values in the SP time series, similar to the process for identifying large spatial differences. Collectively, these number more than 10,000 individual tests; here, we provide an overview of the most interesting results.

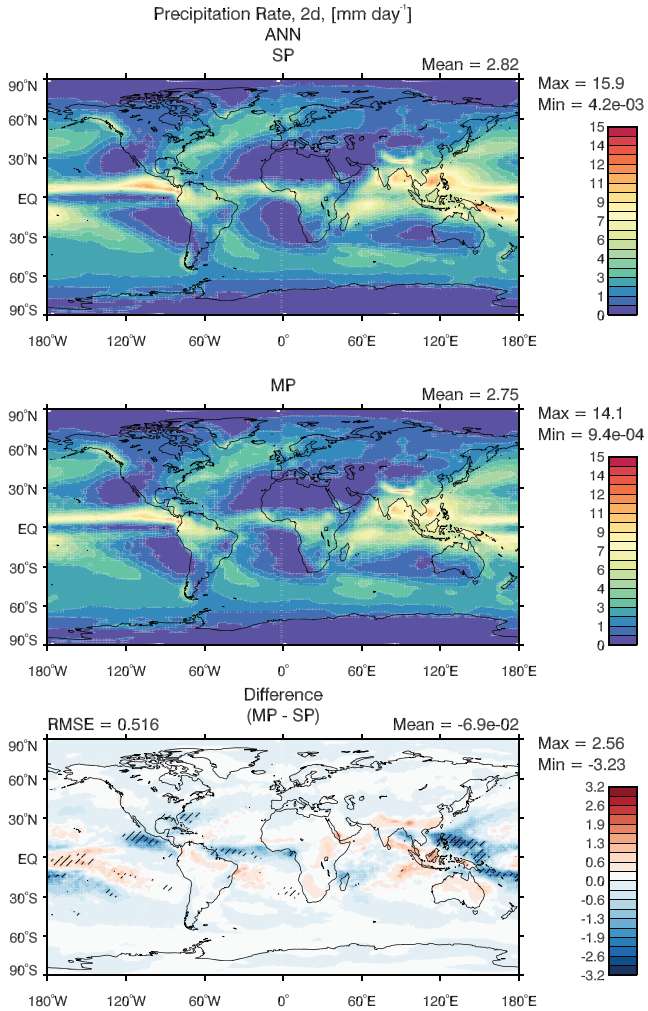

Figure 11. Annual mean precipitation rate for SP (top), MP (middle), and the SP-MP difference (bottom). Diagonal black lines indicate areas of statistically significant differences. SP = superparameterized; MP = multiple-instance superparameterization; RMSE = root-mean-square error.

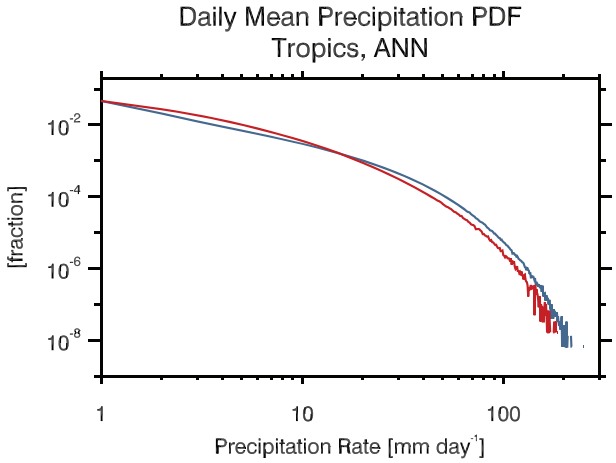

Figure 12. Daily mean precipitation PDFs for superparameterized (blue) and multiple-instance superparameterized (red). PDF = probability density function.

While a number of statistically significant changes in the winds were identified (not shown), the overall pattern of the global circulation agrees well between SP and MP. In most places, the MP zonal winds are slightly stronger than those of SP. The strongest shifts are found at the 100- and 700-hPa levels, where they are on the order of 10%.

As would be expected, these changes in the zonal wind are accompanied by an enhancement of the meridional temperature gradient. MP is cooler in regions poleward of 60° latitude (especially in the south and near the 200-hPa level) are cooler, and MP is warmer by up to about 1 K throughout the tropics (±15° latitude; Figure 6). Temperature increases at 800 hPa act to smooth longitudinal variations at the edge of the tropics (supporting information Figure S3), while increases at 300 hPa are more uniform across the whole of the tropics (supporting information Figure S4), indicating a deepening of the troposphere. This is confirmed by model diagnostics; the global mean tropopause height is about 85 m higher in MP. This difference is not statistically significant with our most stringent test, but it is with all other means tests. Locally, there are increases by as much as 800 m. The deep tropical warming implies an increase in the dry static stability.

Significant changes in specific humidity (Figure 7) are mostly confined to the tropics and subtropics, with moistening at low levels off the equator, meridionally broader drying near the 800-hPa level and stronger, statistically significant moistening in the tropics above 700 hPa. Given the warming shown in Figure 6, the upper-tropospheric increase in specific humidity is qualitatively consistent with constant relative humidity.

4.2. Precipitation

Because each GCM grid column of MP contains 10 CPMs instead of 1, MP has "10 chances" to produce precipitation, while SP has only 1 chance. We find that *the global mean frequency of precipitation increases from*

Table 2
Percentage of Dry Days (Precipitation Less Than 0.1 mm/day) in Each Simulation

Data set	Global	Tropical	TRMM
TRMM	—	38.4	45.9
GPCP	47.7	45.6	48.2
CAM	25.1	16.1	24.2
SP	30.1	22.9	30.1
MP	30.0	22.8	29.6
MP.1	40.7	49.8	48.4

Note. Columns are for global, tropical (20°S to 20°N), and TRMM (50°S to 50°N) regions. TRMM = Tropical Rainfall Measuring Mission; GPCP = Global Precipitation Climatology Project; CAM = Community Atmosphere Model; SP = superparameterized; MP = multiple-instance superparameterization.

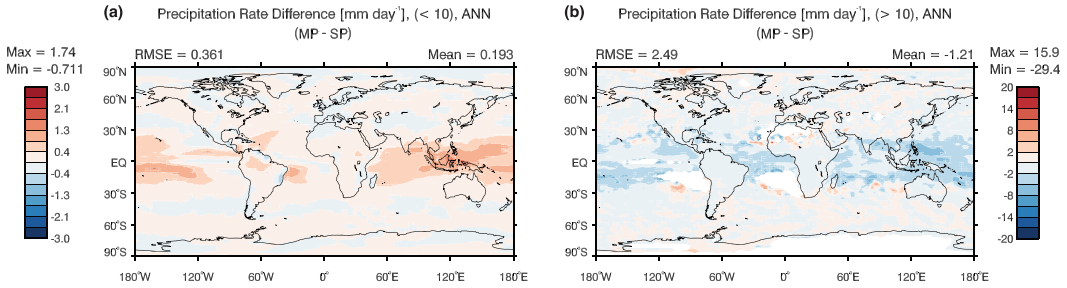

Figure 13. The precipitation rate difference between MP and SP (a) where rates are less than 10 mm/day and (b) where rates are greater than 10 mm/day. SP = superparameterized; MP = multiple-instance superparameterization; RMSE = root-mean-square error.

59–64% to 71–76%, a very strong change that is persistent across all seasons and is significant by all measures (Figure 8). The difference is largest in the tropics (Figure 9), and it is hemispherically asymmetric, with the greatest increase near 30°S. There is not much longitudinal variation (not shown).

Although precipitation occurs more frequently in MP, the global mean precipitation *rate* is lower in MP by about 0.07 mm/day or 2% (Figure 10). This decrease is statistically significant by all measures. It is largest in the tropics (Figure 11); for example, the largest decrease in the tropical Western Pacific is −3.23 mm/day. There are also a few regions of statistically significant precipitation increase over the central equatorial Pacific (maximum magnitude 2.56 mm/day). Viewed seasonally, the major decreases follow the ITCZ.

Recall from section 2.1, the conventional physics parameterization of CAM runs in the background of the superparameterized simulations, recording its convective responses to changes in the GCM state without feeding back to the simulation. The Zhang-McFarlane deep convective scheme also suggests a

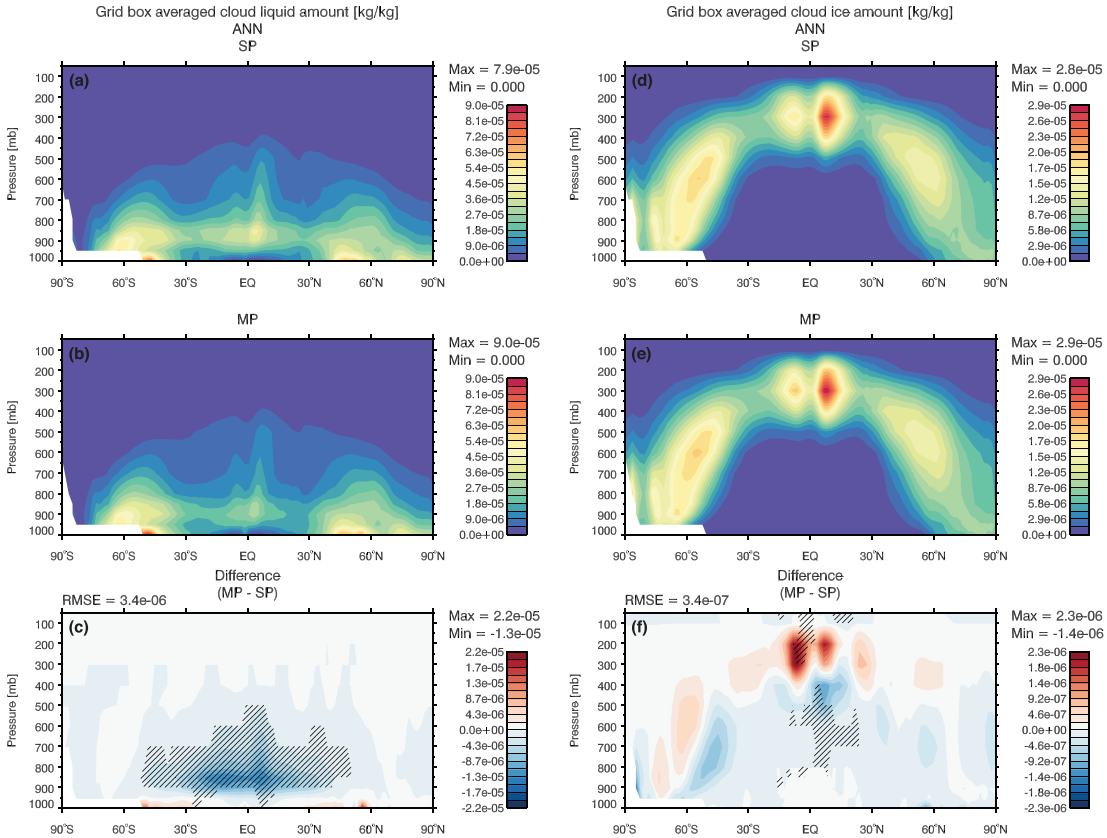

Figure 14. As in Figure 6 but for the grid box-averaged amount of cloud liquid (a–c) and cloud ice (d–f).

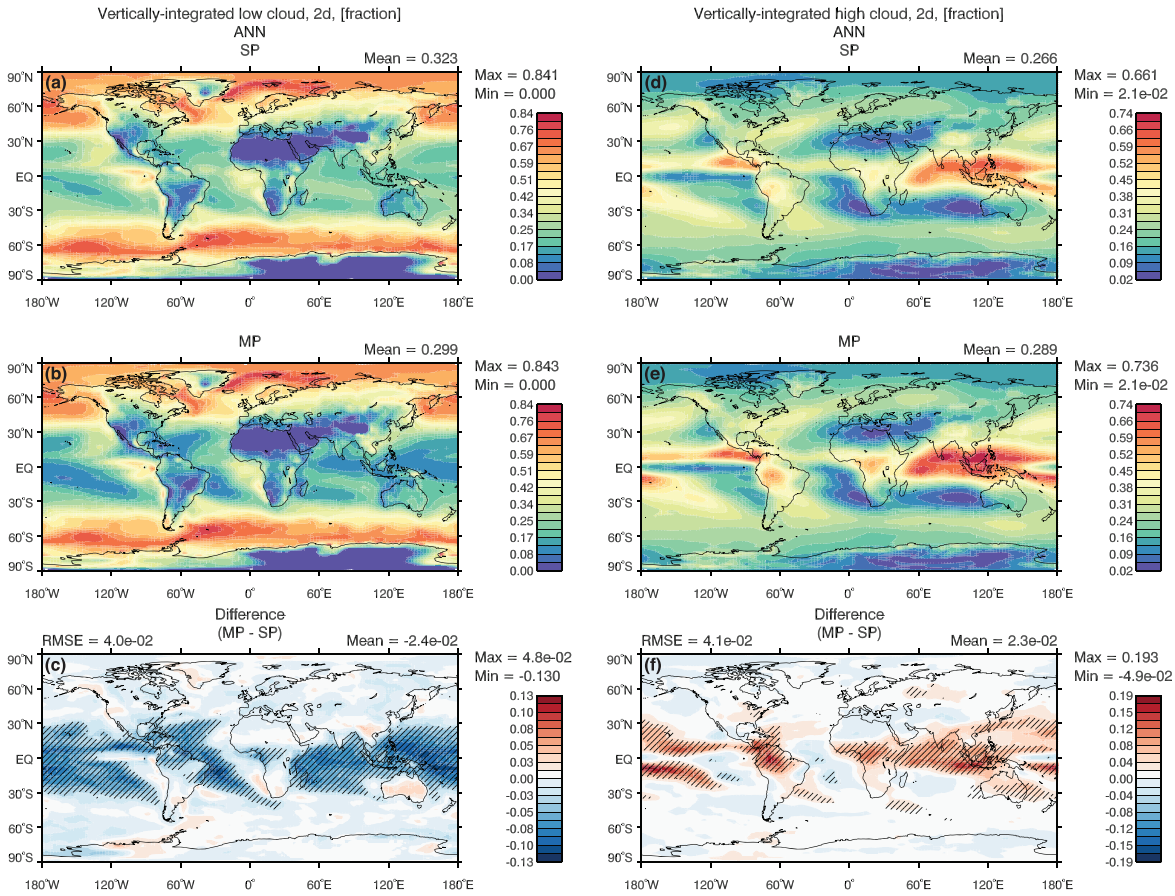

Figure 15. As in Figure 11 but for vertically integrated (a–c) low (surface 700 hPa) and (d–f) high (above 400 hPa) cloud amount.

decrease in heavy convective precipitation in MP relative to SP. In the global mean, the difference is approximately 0.25 mm/day. Additional reductions are associated with the shallow convection scheme of the conventional CAM.

Figure 12 shows the PDFs of the daily mean precipitation rate for the full-length SP and MP data sets in the tropics. As expected, MP produces intense precipitation rates less frequently than SP. MP produces an increase in the frequency of moderate precipitation rates, in the range 1 to 10 mm/day. There are slightly fewer dry days in MP (Table 2). The daily mean precipitation PDFs in TRMM, GPCP, CAM, SP, MP, and MP.1 are shown as a function of latitude in Figure S5. Here, we can see the way in which model differences shown in the previous figure are common across all latitudes, as well as the striking enhancement of the extreme tropical precipitation values in MP.1. The anomalous-looking spike at about 30°N in the model output is due to excessive simulated precipitation over the Himalayas.

Figure 13 shows how these changes are distributed geographically. Light precipitation areas are mostly concentrated in the tropics over the Indian Ocean, across the maritime continent and into the central Pacific, with a notable local maximum off the eastern coast of Brazil. The reduction in heavy precipitation is fairly uniform across the tropics. SP and MP are quite similar in their latitudinal discretization of precipitation PDFs in comparison to the other data sets. In fact, it is a little surprising, given the initial intentions of the MP configuration, that the PDFs do not look more like those from CAM. It is clear from the MP.1 PDFs that individual members of MP's CPM ensemble are behaving differently than the single CPM of SP-CAM. Specifically, the individual members of MP's ensemble produce many more extreme values at all latitudes. This is consistent with the fact, discussed in Part 1, that each individual CPM only provides 10% of the feedback to the GCM, so the total GCM feedback need not be closely tied to any individual CPM. This means that the individual CPMs are less constrained in a quasi-equilibrium sense.

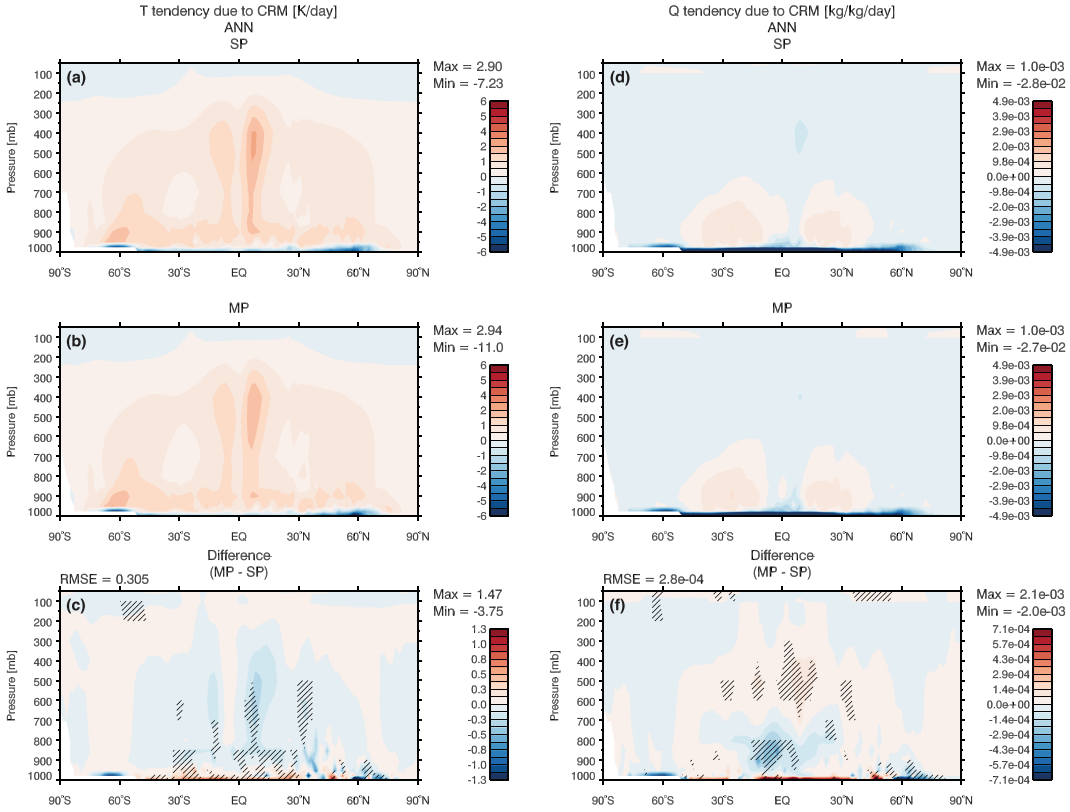

Figure 16. As in Figure 6 but for cloud-permitting model physical tendencies, excluding radiation, of (a–c) temperature and (d–f) specific humidity.

4.3. Cloudiness

Figure 14 shows the annual zonal mean mixing ratios of grid box-averaged cloud liquid and ice. Significant changes include reductions in both cloud liquid and cloud ice at lower levels and an increase in cloud ice above 300 hPa. Both of these changes are strongest in the tropics. The decrease in cloud liquid is slightly stronger in the Southern Hemisphere, and it is strongest and most statistically significant over the oceans. It is mostly absent over land except for regions with frequent deep convection, and it is not seen in the marine subtropical stratus regions. Midlevel reductions in cloud ice are significant mostly because there was so little to begin with. Increases in cloud ice are collocated with the strongest deep convection over both land and ocean.

Model diagnostics define low, middle, and high cloud for the ranges surface 700, 700–400, and above 400 hPa, respectively. Midlevel cloud amounts are statistically unchanged in the global mean, but they do changeby up to ±6% along the ITCZ in the annual mean, with decreases across the Atlantic and western Pacific and increases across the Indian Ocean. The annual mean geographic distribution and differences for low and high clouds are shown in Figure 15. The difference in the global mean time series for both of these variables is statistically significant according to each testing method. The globally averaged low cloud amount decreases from 32% to 30%. Local reductions in low cloud fraction in the tropics exceed 10%. Similarly, these are areas common to deep convection and fair weather cumulus and marine stratocumulus away from the coasts. These are areas where low cloud amount is small in SP.

Globally averaged high cloud amount increases in the annual mean from 26.6% to 28.9%. Increases in the annual mean tropical high cloud amount reach or exceed 10% in many places. The high cloud amount tends to increase where high clouds are prevalent in SP, and it decreases where high cloud amount in SP has local minima. In short, the pattern seen in SP is amplified in MP.

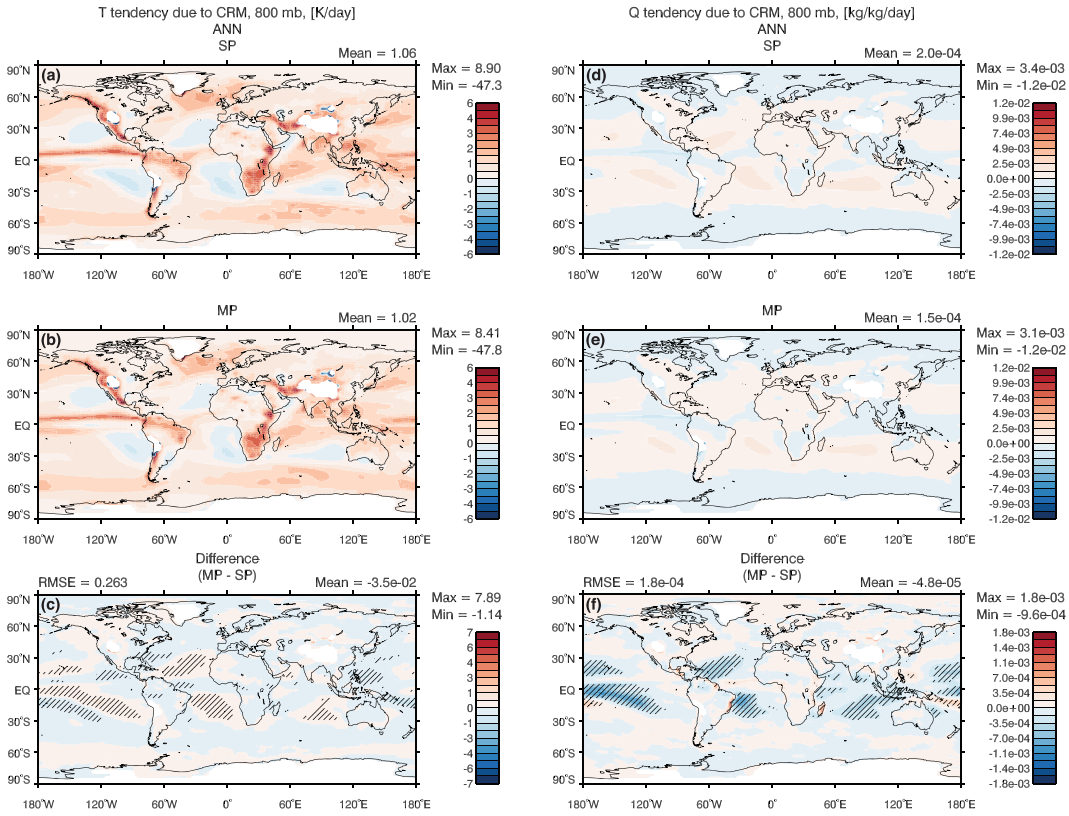

Figure 17. As in Figure 11 but for cloud-permitting model physical tendencies of (a–c) temperature and (d–f) specific humidity at the 800-hPa level.

Test simulations starting SP and MP from identical initial conditions show that the reduction in low cloud amount and the increase in high cloud amount in MP, relative to SP, are apparent after just two simulated days.

Matching the change in high cloud is the change in total precipitable water (not shown), which increases slightly in MP in the global mean, but significantly where there has been an increase in high cloud amount. Cloud water path (including both liquid and ice) follows the loss of low cloud in MP, as liquid water path losses heavily outweigh gains in ice water path, which only barely register as statistically significant. All of these changes hold regardless of season. The global total cloud fraction increases by 0.2%, with marginal statistical significance.

Since low clouds cool radiatively by scattering solar radiation, and high clouds warm radiatively by trapping terrestrial radiation, the decrease in low cloudiness and the increase in high cloudiness work in the same direction in terms of the column-integrated cloud radiative effect (CRE), which is defined as the difference between the radiative fluxes or heating rates for all-sky and clear-sky conditions. Globally, the top-of-atmosphere shortwave CRE increases (i.e., becomes less negative) by about 3 W/m^2 in association with reduced low cloud amount, and longwave CRE increases by almost 2 W/m^2 due to increases in high cloud amount. Because of these strengthened radiative effects, the atmosphere is cooling more slowly in MP than in SP. Since atmospheric cooling by radiation is ultimately balanced by condensational heating, the decrease in global mean precipitation is consistent with and may be caused by the changes in the high cloudiness.

What causes the changes in cloudiness? As discussed earlier in this section, ensemble averaging leads to more frequent, less intense precipitation, because with 10 CPMs there are 10 chances for precipitation. The more frequent ensemble-averaged precipitation is accompanied by greater ensemble-averaged high cloudiness in the regions where precipitation increases.

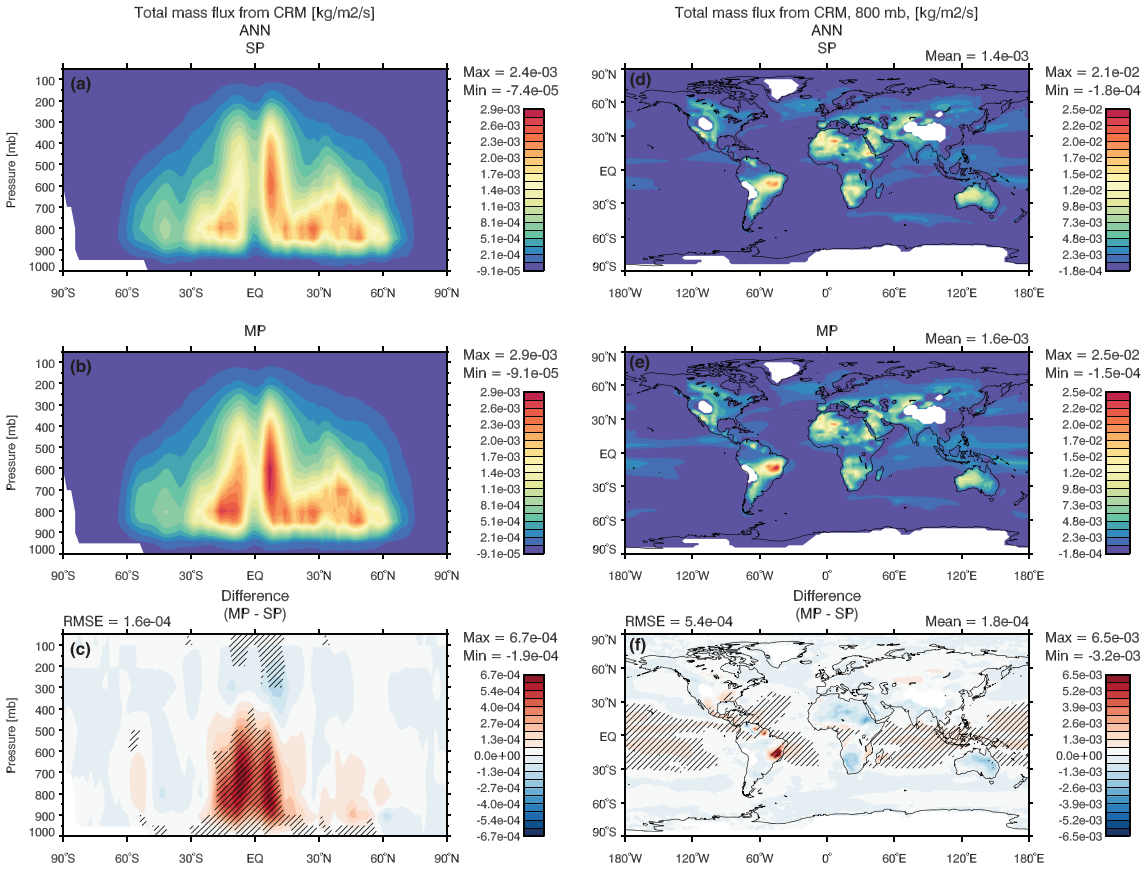

Figure 18. As in Figures 6 and 11 but for (a–c) the zonal annual mean of the cloud-permitting model total mass flux and (d–f) its annual mean at the 800 hPa level.

In addition to reducing the OLR, high clouds increase the downwelling infrared radiation in the lower troposphere. An increase in downwelling infrared radiation from the middle and/or upper troposphere reduces the rate of radiative cooling at the tops of low clouds and so leads to a decrease in low cloud amount (e.g., Bretherton, 2015; Christensen et al., 2013).

4.4. Heating and Drying Rates

We had to consider the effects of ensemble averaging on precipitation in order to understand the changes in the frequency of occurrence of extreme precipitation. The same must be done for the heating and drying rates fed back to the GCM. Not only are they smoother in time and in the vertical in MP compared to SP but their extremes are diminished through the ensemble averaging procedure. Figure 16 shows the annual zonal mean for the temperature and specific humidity tendencies from the CPM level in SP and MP and their difference. Both SP and MP warm and dry the troposphere via condensation and convective transports, but since the MP tendencies are derived from an average, there are systematic differences.

Figure 16 shows the heating and drying due to CPM processes other than radiation. It is apparent that through most of the troposphere MP produces less warming and drying than SP. This is consistent with MP's reduced rates of radiative cooling and precipitation. What cannot be clearly seen in Figure 16, however, is that MP has anomalous (compared to SP) drying and heating (i.e., reduced cooling) at the level of the low clouds (Figure 17). This decrease in the low-level radiative cooling rate reduces the low-level divergence (not shown). It is consistent with the radiative effects of increase high clouds.

Despite the fact that MP simulates weaker nonradiative heating and drying rates, it produces stronger mass fluxes within the CPM (Figure 18). The largest value in the annual zonal mean of MP is nearly 25% greater than that in SP. This is the strongest relative change in the annual zonal mean of any

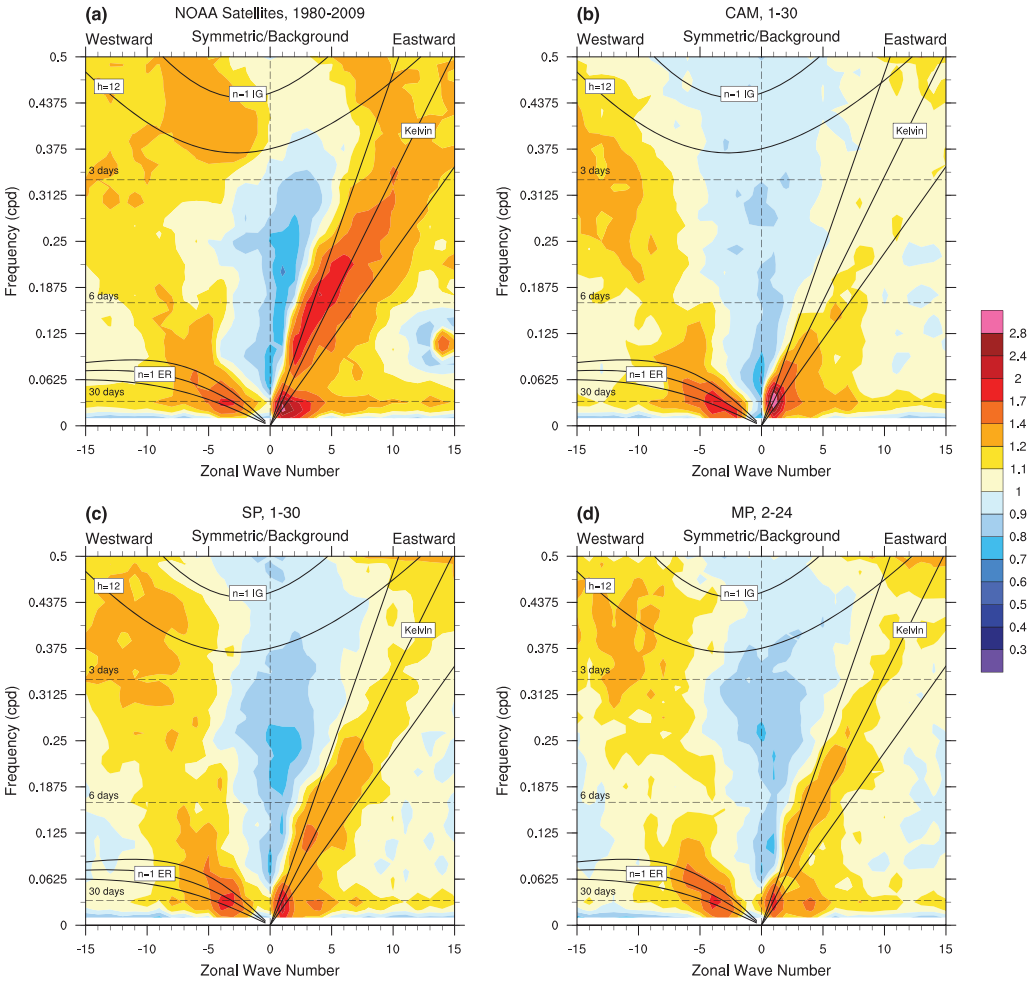

Figure 19. Ratios of symmetric spectral power to a smoothed background power for outgoing longwave radiation for (a) NOAA observations, (b) CAM, (c) SP-CAM, and (d) MP-CAM. Dispersion curves of the linear shallow water equations are shown in solid black for equivalent depths of 12, 25, and 50 m. Wave types are equatorial Rossby (ER), inertia-gravity (IG), and Kelvin. NOAA = National Oceanic and Atmospheric Administration; CAM = Community Atmosphere Model; SP = superparameterized; MP = multiple-instance superparameterization.

variable that we have analyzed. The stronger mass fluxes of MP would by themselves produce stronger CPM heating and drying rates. The fact that the heating and drying rates are actually weaker in MP indicates that the cooling and moistening associated with the evaporation of stratiform precipitation are stronger in MP than in SP. This is consistent with the larger high cloud fraction and precipitable water of MP.

Despite a variety of statistically significant shifts in simulated climate in MP relative to SP, the changes do not represent a wild departure from SP or from other models in general. Of particular interest is that MP shows some measurable reduction in variability relative to SP, as expected. Jones (2017) demonstrates the ability of MP to reproduce some observed aspects of convective variability, consistent with analyses by Peters et al. (2013), Davies et al. (2013), and Watson et al. (2014).

5. Intraseasonal Variability

The final item to address is the simulated intraseasonal variability, particularly as represented by the MJO. While many atmospheric models have had difficulty in accurately simulating the MJO, SP-CAM has been relatively successful. Can its more deterministic offshoot, MP-CAM, also simulate the MJO? As mentioned in section 1, it has been suggested that stochastic convective variability plays a significant role in a model's

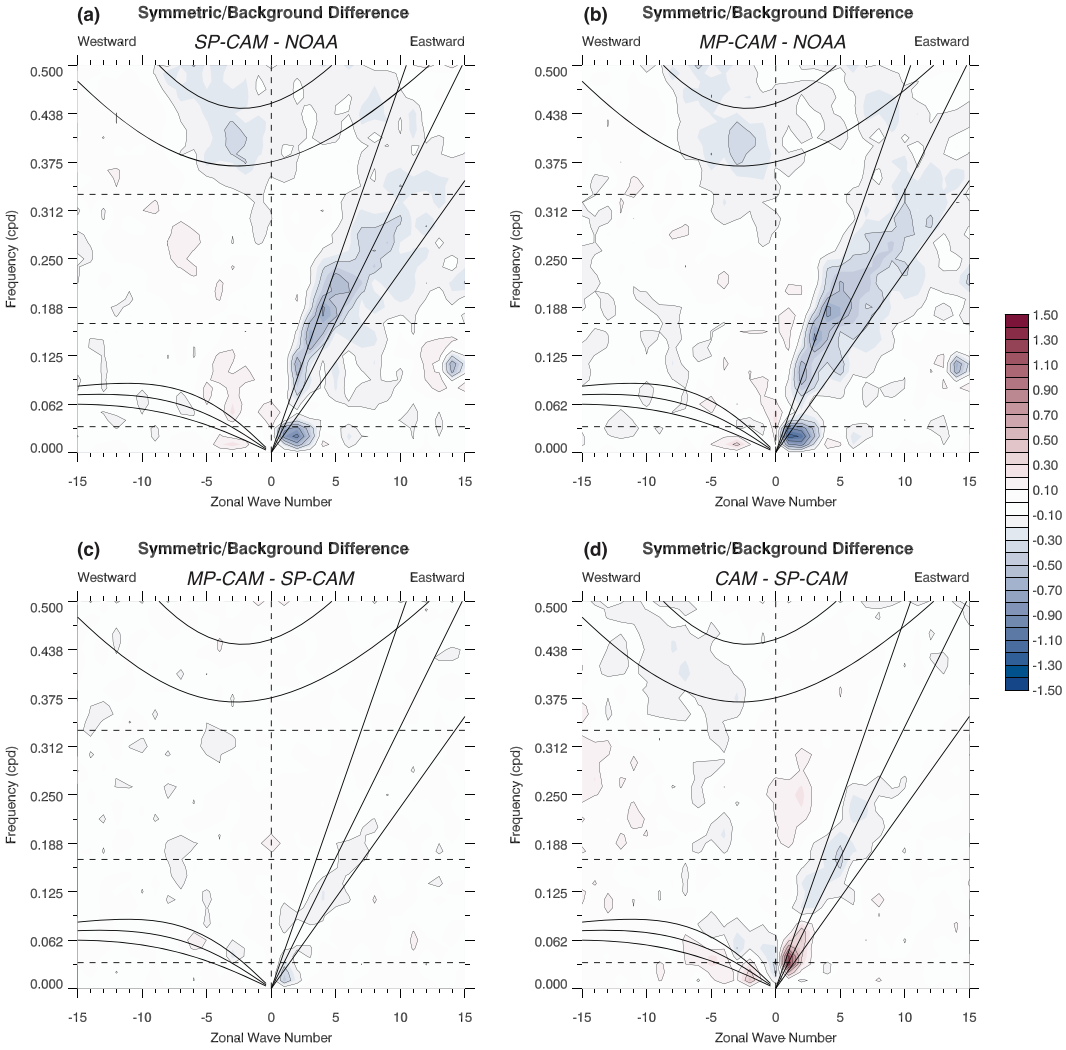

Figure 20. Differences in the ratios of symmetric spectral power to a smoothed background power for outgoing longwave radiation as shown in Figure 19 for (a) SP-CAM and NOAA observations, (b) MP-CAM and NOAA observations, (c) MP-CAM and SP-CAM, and (d) CAM and SP-CAM. SP = superparameterized; CAM = Community Atmosphere Model; NOAA = National Oceanic and Atmospheric Administration; MP = multiple-instance superparameterization.

ability to produce a realistic MJO. In order to evaluate the MJO in SP and MP, we have relied heavily on the diagnostic tools described by Waliser et al. (2009). Relevant variables for the analysis are precipitation rate, OLR, and zonal wind at 850 hPa. While each of these variables is available for the entirety of the SP simulation, all of them are only available for MP from year 4 onward.

Hovmöller diagrams (not shown) of 20- to 80-day band-pass filtered OLR anomalies, meridionally averaged from 10°S to 5°N latitude, show slightly greater MJO activity in SP case. Perhaps the most common way to reveal the MJO signal is through zonal wave number-frequency analysis as pioneered by Wheeler and Kiladis (1999). We used a frequency spectral bandwidth of 1/96 cycles per day with a 65-day temporal segment overlap. Figure 19 shows the results for symmetric (across the equator) variability of the OLR, for data within ±15° latitude in NOAA observations, CAM, SP, and MP. The MJO is represented by the region of strong spectral power for eastward (positive) zonal wave numbers 1–2, below the 30-day period dashed lines. Understanding that the background spectra are approximately the same in each case, the first thing to note is that wave activity is generally weaker than observed in all cases. CAM actually produces the largest model signal near the MJO; however, much of this peak is placed at incorrect, higher frequencies. CAM is also notably deficient in its representation of Kelvin wave activity.

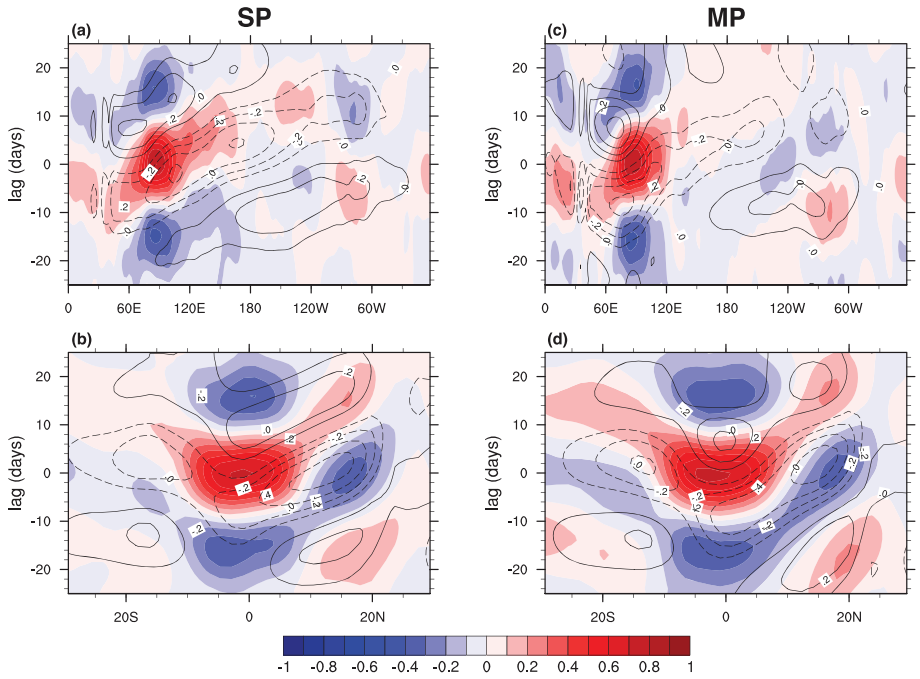

Figure 21. Lag correlation diagrams based on filtered daily data as described in the text, considering the annual precipitation time series for (a, b) SP and (c, d) MP in the (a, c) zonal and (b, d) meridional directions. Precipitation anomalies are shown in colors, and 850-hPa zonal wind anomalies are contoured in lines. SP = superparameterized; MP = multiple-instance superparameterization.

SP and MP appear roughly equivalent at first glance. Both have overall weaker and slightly different signals than the observations, though we should bear in mind that these model runs do not have the advantage of interactive sea surface temperatures, which play a significant role in modulating the MJO (de Boisséson et al., 2012; DeMott et al., 2015; Wang et al., 2015). Figure 20 shows difference plots for the data in Figure 19. The SP and MP differences from the NOAA observations are strikingly similar overall. Both appear to lack power in the Kelvin wave and MJO regions of the spectrum, with a smaller deficiency along the inertia-gravity wave dispersion curves. Comparing the results of MP and SP more directly (bottom, left), we see that the two models are producing very similar results overall. MP has a slightly weaker Kelvin wave signal and a much weaker MJO signal. While SP shows strongest difference from observations at wave number 2 with less discrepancy at wave number 1, the deficiency in MP is more evenly distributed across those two wave numbers with a slightly stronger deviation at wave number 1.

The MP peak difference corresponds to an approximately 10% reduction in the spectral power ratio, which is strong enough to be considered significant. On the other hand, the overall shape of the power spectrum has not changed significantly. For instance, the CAM representation of the MJO spectral power signal, while also too tightly confined to wave number 1, is shifted to higher-frequency modes, moving into the Kelvin wave range. By this measure, the MP simulation shows only slight degradation of the MJO signal. The caveat here is that these diagnostics are performed on the OLR data, which we have shown to be unexpectedly variable in MP despite the averaging effects of the CPM ensemble due to slight changes in the climatology. Further evidence for the decline in MJO activity is shown in phase activity diagrams of the real-time multivariate MJO index (Wheeler & Hendon, 2004), available in the supporting information (Figure S6). They show a greater frequency of occurrence at weak amplitudes and less frequent occurrence at strong amplitudes in MP.

Finally, we look at lag correlation diagrams (Figure 21), which show the composite motion of the MJO considered from an annual perspective. Summer and winter perspectives are shown in the supporting information (Figures S7 and S8). The lag is defined with respect to peak precipitation in the central Indian Ocean, where the MJO originates. This time series is correlated with precipitation and zonal wind anomalies from ±10° latitude and 80–100° longitude that have been band-pass filtered for the range of 20–100 days. Here the

color is precipitation and the line contours are the zonal winds at 850 hPa. Meridional propagation is quite similar in SP and MP, though MP is slightly faster. For zonal propagation, however, there are some clear differences. Relative to SP, in MP the disturbance does not propagate as far to the east nor does it maintain its intensity. The MP precipitation anomalies stop at about 120°E, and the trailing anomalies propagate more quickly westward toward the prime meridian than those in SP. Observed anomalies (not shown) closely match the pattern of SP in both directions, although they are stronger. The MP representation of MJO propagation is markedly inferior to that of SP.

6. Conclusions

The work described here and by Jones et al. (2019) demonstrates a novel modeling technique that we have used to uncover statistical relationships between the predictability of precipitation and characteristics of the large-scale circulation as simulated by a GCM. MP-CAM allows us to analyze multiple realizations that are consistent with a single, evolving large-scale state. We created MP to test the performance of a deterministic parameterization, obtained by averaging the physical tendencies produced by the multiple stochastic CPMs. We have shown that MP is in fact more deterministic than SP.

The 10 CPMs of MP provide 10 chances for precipitation and 10 chances for high-level cloudiness in each grid column of MP-CAM, on each time step. As a direct result, the frequency of precipitation and the frequency of high cloudiness both increase in MP, relative to SP. The increased *frequency* of high cloudiness leads to an increase in high cloud *amount*. The increased high cloud amount reduces the OLR and also reduces the rate at which the troposphere is cooled by radiation. From the point of view of energy balance, the reduced radiative cooling of the troposphere explains why the globally averaged precipitation rate is smaller in MP than in SP. The increased high cloudiness also increases the flux of downwelling longwave radiation from the upper troposphere. This leads to a reduction in low cloud amount, which weakens the planetary cooling effects of the shortwave CRE. Since the longwave and shortwave effects of MP both tend to warm, we speculate that in coupled ocean-atmosphere simulations MP would produce a warmer planet than SP. Individually, the 10 CPMs of MP are less constrained than the single CPM of SP, permitting them to represent a wider range of realizations of a given GCM state. Because of this and internal feedbacks, they can even produce different average climatological behavior in some locations, though the effect is typically small.

MP's simulation of the MJO is not as realistic as that of SP. In particular, the MJO's spectral power is slightly reduced, and it has spatially limited and unrealistically rapid propagation. Kelvin wave activity is also more realistic in SP than in MP. Our results support the idea that stochastic effects can help to produce realistic simulation of the these tropical weather systems (Neelin et al., 2008).

Acknowledgments
Todd Jones was supported by a CIRA Graduate Student Fellowship. The encouragement of Prof. Christian Kummerow is gratefully acknowledged. Additional support was provided by the National Science Foundation Science and Technology Center for Multiscale Modeling of Atmospheric Processes, managed by Colorado State University under cooperative Agreement ATM-0425247. Computing resources were provided by NCAR's Computational and Information Systems Laboratory, sponsored by the National Science Foundation. Additional support was provided by the National Oceanic and Atmospheric Administration under Grant NA16OAR4590230 to Colorado State University. The authors thank Nicholas Klingaman for technical support and helpful discussions. The authors thank two anonymous reviewers for their helpful comments. The authors have arranged for the data to be made available from the Mountain Scholar institutional repository managed by Colorado State University. It can be accessed online (https://hdl.handle.net/10217/195181).

References

Arakawa, A. (2004). The cumulus parameterization problem: Past, present, and future. *Journal of Climate*, *17*(13), 2493–2525. https://doi.org/10.1175/1520-0442(2004)017<2493:RATCPP>2.0.CO;2

Bauer, P., Thorpe, A., & Brunet, G. (2015). The quiet revolution of numerical weather prediction. *Nature*, *525*(7567), 47–55. https://doi.org/10.1038/nature14956

Bechtold, P., Semane, N., Lopez, P., Chaboureau, J.-P., Beljaars, A., & Bormann, N. (2013). Representing equilibrium and nonequilibrium convection in large-scale models. *Journal of the Atmospheric Sciences*, *71*(2), 734–753. https://doi.org/10.1175/JAS-D-13-0163.1

Berner, J., Achatz, U., Batté, L., Bengtsson, L., Cámara, A. d. l., Christensen, H. M., et al. (2017). Stochastic parameterization: Toward a new view of weather and climate models. *Bulletin of the American Meteorological Society*, *98*(3), 565–588. https://doi.org/10.1175/BAMS-D-15-00268.1

Berner, J., Fossell, K. R., Ha, S. Y., Hacker, J. P., & Snyder, C (2015). Increasing the skill of probabilistic forecasts: Understanding performance improvements from model-error representations. *Monthly Weather Review*, *143*(4), 1295–1320. https://doi.org/10.1175/MWR-D-14-00091.1

Berner, J., Jung, T., & Palmer, T. N. (2012). Systematic model error: The impact of increased horizontal resolution versus improved stochastic and deterministic parameterizations. *Journal of Climate*, *25*(14), 4946–4962. https://doi.org/10.1175/JCLI-D-11-00297.1

Bowler, N. E., Arribas, A., Beare, S. E., Mylne, K. R., & Shutts, G. J (2009). The local ETKF and SKEB: Upgrades to the MOGREPS short-range ensemble prediction system. *Quarterly Journal of the Royal Meteorological Society*, *135*(640), 767–776. https://doi.org/10.1002/qj.394

Bretherton, C. S (2015). Insights into low-latitude cloud feedbacks from high-resolution models. *Philosophical Transactions of the Royal Society A: Mathematical, Physical and Engineering Sciences*, *373*(2054), 20140415. https://doi.org/10.1098/rsta.2014.0415

Bretherton, C. S., Widmann, M., Dymnikov, V. P., Wallace, J. M., & Bladé, I (1999). The effective number of spatial degrees of freedom of a time-varying field. *Journal of Climate*, *12*(7), 1990–2009. https://doi.org/10.1175/1520-0442(1999)012<1990:TENOSD>2.0.CO;2

Buizza, R., Miller, M., & Palmer, T. N. (1999). Stochastic representation of model uncertainties in the ECMWF ensemble prediction system. *Quarterly Journal of the Royal Meteorological Society*, *125*(560), 2887–2908. https://doi.org/10.1002/qj.49712556006

Charron, M., Pellerin, G., Spacek, L., Houtekamer, P. L., Gagnon, N., Mitchell, H. L., & Michelin, L. (2010). Toward random sampling of model error in the Canadian Ensemble Prediction System. *Monthly Weather Review*, *138*(5), 1877–1901. https://doi.org/10.1175/2009MWR3187.1

Chen, B., Li, J., & Ding, R. (2006). Nonlinear local Lyapunov exponent and atmospheric predictability research. *Science in China Series D: Earth Sciences*, *49*(10), 1111–1120. https://doi.org/10.1007/s11430-006-1111-0

Christensen, M. W., Carrió, G. G., Stephens, G. L., & Cotton, W. R. (2013). Radiative impacts of free-tropospheric clouds on the properties of marine stratocumulus. *Journal of the Atmospheric Sciences*, *70*(10), 3102–3118. https://doi.org/10.1175/JAS-D-12-0287.1

Davies, L., Jakob, C., May, P., Kumar, V. V., & Xie, S. (2013). Relationships between the large-scale atmosphere and the small-scale convective state for Darwin, Australia. *Journal of Geophysical Research: Atmospheres*, *118*, 11,534–11,545. https://doi.org/10.1002/jgrd.50645

Davini, P., von Hardenberg, J., Corti, S., Christensen, H. M., Juricke, S., Subramanian, A., et al. (2017). Climate sphinx: Evaluating the impact of resolution and stochastic physics parameterisations in the EC-Earth global climate model. *Geoscientific Model Development*, *10*(3), 1383–1402. https://doi.org/10.5194/gmd-10-1383-2017

de Boisséson, E., Balmaseda, M. A., Vitart, F., & Mogensen, K. (2012). Impact of the sea surface temperature forcing on hindcasts of Madden-Julian Oscillation events using the ECMWF model. *Ocean Science*, *8*(6), 1071–1084. https://doi.org/10.5194/os-8-1071-2012

DeMott, C. A., Klingaman, N. P., & Woolnough, S. J. (2015). Atmosphere-ocean coupled processes in the Madden-Julian oscillation. *Reviews of Geophysics*, *53*, 1099–1154. https://doi.org/10.1002/2014RG000478

DeMott, C. A., Randall, D. A., & Khairoutdinov, M. (2007). Convective precipitation variability as a tool for general circulation model analysis. *Journal of Climate*, *20*(1), 91–112. https://doi.org/10.1175/JCLI3991.1

Ding, R., Li, J., & Ha, K.-J. (2008). Trends and interdecadal changes of weather predictability during 1950s–1990s. *Journal of Geophysical Research*, *113*, D24112. https://doi.org/10.1029/2008JD010404

Donner, L. J., & Phillips, V. T. (2003). Boundary layer control on convective available potential energy: Implications for cumulus parameterization. *Journal of Geophysical Research*, *108*(D22), 4701. https://doi.org/10.1029/2003JD003773

Epstein, E. S. (1969). Stochastic dynamic prediction. *Tellus*, *21*(6), 739–759. https://doi.org/10.1111/j.2153-3490.1969.tb00483.x

Flato, G., Marotzke, J., Abiodun, B., Braconnot, P., Chou, S., Collins, W., et al. (2013). Evaluation of climate models. In T. Stocker (Ed.), *Climate change 2013: The physical science basis. Contribution of working group I to the fifth assessment report of the intergovernmental panel on climate change* (pp. 741–866). Cambridge, United Kingdom and New York, NY, USA: Cambridge University Press. https://doi.org/10.1017/CBO9781107415324.020

Gehne, M., Hamill, T. M., Kiladis, G. N., & Trenberth, K. E. (2016). Comparison of global precipitation estimates across a range of temporal and spatial scales. *Journal of Climate*, *29*(21), 7773–7795. https://doi.org/10.1175/JCLI-D-15-0618.1

Grabowski, W. W. (2001). Coupling cloud processes with the large-scale dynamics using the Cloud-Resolving Convection Parameterization (CRCP). *Journal of the Atmospheric Sciences*, *58*(9), 978–997. https://doi.org/10.1175/1520-0469(2001)058<0978:CCPWTL>2.0.CO;2

Grabowski, W. W., & Smolarkiewicz, P. K. (1999). CRCP: A cloud resolving convection parameterization for modeling the tropical convecting atmosphere. *Physica D*, *133*(1–4), 171–178. https://doi.org/10.1016/S0167-2789(99)00104-9

Grassberger, P., & Procaccia, I. (1983). Characterization of strange attractors. *Physical Review Letters*, *50*(5), 346–349. https://doi.org/10.1103/PhysRevLett.50.346

Gregory, D., Kershaw, R., & Inness, P. M. (1997). Parametrization of momentum transport by convection. II: Tests in single-column and general circulation models. *Quarterly Journal of the Royal Meteorological Society*, *123*(541), 1153–1183. https://doi.org/10.1002/qj.49712354103

Hack, J. J. (1994). Parameterization of moist convection in the National Center for Atmospheric Research community climate model (CCM2). *Journal of Geophysical Research*, *99*, 5551–5568. https://doi.org/10.1029/93JD03478

Harnisch, F., & Keil, C. (2015). Initial conditions for convective-scale ensemble forecasting provided by ensemble data assimilation. *Monthly Weather Review*, *143*(5), 1583–1600. https://doi.org/10.1175/MWR-D-14-00209.1

Hasselmann, K. (1976). Stochastic climate models Part I. Theory. *Tellus*, *28*(6), 473–485. https://doi.org/10.1111/j.2153-3490.1976.tb00696.x

Hohenegger, C., & Schär, C. (2007). Atmospheric predictability at synoptic versus cloud-resolving scales. *Bulletin of the American Meteorological Society*, *88*(11), 1783–1793. https://doi.org/10.1175/BAMS-88-11-1783

Huffman, G. J., Adler, R. F., Morrissey, M. M., Bolvin, D. T., Curtis, S., Joyce, R., et al. (2001). Global precipitation at one-degree daily resolution from multisatellite observations. *Journal of Hydrometeorology*, *2*(1), 36–50. https://doi.org/10.1175/1525-7541(2001)002<0036:GPAODD>2.0.CO;2

Huffman, G. J., Bolvin, D. T., Nelkin, E. J., Wolff, D. B., Adler, R. F., Gu, G., et al. (2007). The TRMM multisatellite precipitation analysis (TMPA): Quasi-global, multiyear, combined-sensor precipitation estimates at fine scales. *Journal of Hydrometeorology*, *8*(1), 38–55. https://doi.org/10.1175/JHM560.1

Jakob, C. (2014). Going back to basics. *Nature Climate Change*, *4*(12), 1042–1045. https://doi.org/10.1038/nclimate2445

Jones, P. W. (1999). First- and second-order conservative remapping schemes for grids in spherical coordinates. *Monthly Weather Review*, *127*(9), 2204–2210. https://doi.org/10.1175/1520-0493(1999)127<2204:FASOCR>2.0.CO;2

Jones, T. R. (2017). Examining chaotic convection with super-parameterization ensembles (PhD Dissertation), Colorado State University, Fort Collins, CO.

Jones, T. R., & Randall, D. A. (2011). Quantifying the limits of convective parameterizations. *Journal of Geophysical Research*, *116*, D08210. https://doi.org/10.1029/2010JD014913

Jones, T. R., Randall, D. A., & Branson, M. D. (2019). Multiple-instance superparameterization. 1: Concept, and predictability of precipitation. *Journal of Advances in Modeling Earth Systems, 11, 3497 − 3520.* https://doi.org/10.1029/2019ms001610

Khairoutdinov, M. F., & Randall, D. A. (2001). A cloud resolving model as a cloud parameterization in the NCAR Community Climate System Model: Preliminary results. *Geophysical Research Letters*, *28*, 3617–3620. https://doi.org/10.1029/2001GL013552

Khairoutdinov, M., Randall, D., & DeMott, C. (2005). Simulations of the atmospheric general circulation using a cloud-resolving model as a superparameterization of physical processes. *Journal of the Atmospheric Sciences*, *62*(7), 2136–2154. https://doi.org/10.1175/JAS3453.1

Khairoutdinov, M., & Zhou, X. (2015). Changes in sub-daily precipitation extremes in a global climate model with super-parameterization under CO2 warming, *EGU general assembly conference abstracts* (Vol. 17, pp. 7931). Vienna, Austria.

Kim, D., Sperber, K., Stern, W., Waliser, D., Kang, I. S., Maloney, E., et al. (2009). Application of MJO simulation diagnostics to climate models. *Journal of Climate*, *22*(23), 6413–6436. https://doi.org/10.1175/2009JCLI3063.1

Kooperman, G. J., Pritchard, M. S., Burt, M. A., Branson, M. D., & Randall, D. A. (2016). Robust effects of cloud superparameterization on simulated daily rainfall intensity statistics across multiple versions of the Community Earth System Model. *Journal of Advances in Modeling Earth Systems*, *8*, 140–165. https://doi.org/10.1002/2015MS000574

Leith, C. E. (1974). Theoretical skill of Monte Carlo forecasts. *Monthly Weather Review*, *102*(6), 409–418. https://doi.org/10.1175/1520-0493(1974)102<0409:TSOMCF>2.0.CO;2

Li, F., Rosa, D., Collins, W. D., & Wehner, M. F. (2012). "Super-parameterization": A better way to simulate regional extreme precipitation? *Journal of Advances in Modeling Earth Systems*, *4*, M04002. https://doi.org/10.1029/2011MS000106

Liebmann, B., & Smith, C. A. (1996). Description of a complete (interpolated) outgoing longwave radiation dataset. *Bulletin of the American Meteorological Society*, *77*(6), 1275–1277.

Lin, J.-L., Kiladis, G. N., Mapes, B. E., Weickmann, K. M., Sperber, K. R., Lin, W., et al. (2006). Tropical intraseasonal variability in 14 IPCC AR4 climate models. Part I: Convective signals. *Journal of Climate*, *19*(12), 2665–2690. https://doi.org/10.1175/JCLI3735.1

Liu, J., Li, W., Chen, L., Zuo, J., & Zhang, P. (2016). Estimation of the monthly precipitation predictability limit in China using the non-linear local Lyapunov exponent. *Journal of Meteorological Research*, *30*(1), 93–102. https://doi.org/10.1007/s13351-015-5049-z

Lorenz, E. N. (1969). The predictability of a flow which possesses many scales of motion. *Tellus*, *21*(3), 289–307. https://doi.org/10.1111/j.2153-3490.1969.tb00444.x

Millán, H., Kalauzi, A., Llerena, G., Sucoshañay, J., & Piedra, D. (2009). Meteorological complexity in the Amazonian area of Ecuador: An approach based on dynamical system theory. *Ecological Complexity*, *6*(3), 278–285. https://doi.org/10.1016/j.ecocom.2009.05.004

Millán, H., Rodríguez, J., Ghanbarian-Alavijeh, B., Biondi, R., & Llerena, G. (2011). Temporal complexity of daily precipitation records from different atmospheric environments: Chaotic and Lévy stable parameters. *Atmospheric Research*, *101*(4), 879–892. https://doi.org/10.1016/j.atmosres.2011.05.021

Molteni, F., Buizza, R., Palmer, T. N., & Petroliagis, T. (1996). The ECMWF ensemble prediction system: Methodology and validation. *Quarterly Journal of the Royal Meteorological Society*, *122*(529), 73–119. https://doi.org/10.1002/qj.49712252905

Mureau, R., Molteni, F., & Palmer, T. N. (1993). Ensemble prediction using dynamically conditioned perturbations. *Quarterly Journal of the Royal Meteorological Society*, *119*(510), 299–323. https://doi.org/10.1002/qj.49711951005

NOAA National Centers for Environmental Information (NCEI) U.S. (2019). Billion-Dollar Weather and Climate Disasters. https://www.ncdc.noaa.gov/billions/

Neale, R. B., Chen, C.-C., Gettelman, A., Lauritzen, P. H., Park, S., Williamson, D. L., et al. (2012). Description of the NCAR Community Atmosphere Model (CAM 5.0) (NCAR technical note NCAR/TN-486+STR). Boulder, Colorado, USA: NCAR.

Neale, R. B., Richter, J. H., Conley, A. J., Park, S., Lauritzen, P. H., Gettelman, A., et al. (2010). Description of the NCAR Community Atmosphere Model (CAM 4.0) (NCAR Tech. Note NCAR/TN-485+STR). Boulder, Colorado, USA: NCAR.

Neale, R. B., Richter, J. H., & Jochum, M. (2008). The impact of convection on ENSO: From a delayed oscillator to a series of events. *Journal of Climate*, *21*(22), 5904–5924. https://doi.org/10.1175/2008JCLI2244.1

Neelin, J. D., Peters, O., Lin, J. W. B., Hales, K., & Holloway, C. E. (2008). Rethinking convective quasi-equilibrium: Observational constraints for stochastic convective schemes in climate models. *Philosophical Transactions of the Royal Society A: Mathematical, Physical and Engineering Sciences*, *366*(1875), 2581–2604. https://doi.org/10.1098/rsta.2008.0056

Palmer, T. N. (2000). Predicting uncertainty in forecasts of weather and climate. *Reports on Progress in Physics*, *63*(2), 71–116. https://doi.org/10.1088/0034-4885/63/2/201

Palmer, T. N., Molteni, F., Mureau, R., Buizza, R., Chapelet, P., & Tribbia, J. (1993). Ensemble prediction, *Seminar proceedings on validation of models over Europe* (Vol. 1, pp. 285). Shinfield Park, Reading, UK.

Peters, K., Jakob, C., Davies, L., Khouider, B., & Majda, A. J. (2013). Stochastic behavior of tropical convection in observations and a multicloud model. *Journal of the Atmospheric Sciences*, *70*(11), 3556–3575. https://doi.org/10.1175/JAS-D-13-031.1

Randall, D., DeMott, C., Stan, C., Khairoutdinov, M., Benedict, J., McCrary, R., et al. (2016). Simulations of the tropical general circulation with a multiscale global model. *Meteorological Monographs*, *56*, 15.1–15.15. https://doi.org/10.1175/AMSMONOGRAPHS-D-15-0016.1

Randall, D. A., & Ding, P. D.-M. P. (1997). Quasi-equilibrium, *The physics and parameterization of moist atmospheric convection* (pp. 359–385). The Netherlands: Kluwer Academic Publishers.

Randall, D. A., Hu, Q., Xu, K. M., & Krueger, S. K. (1994). Radiative-convective disequilibrium. *Atmospheric Research*, *31*(4), 315–327. https://doi.org/10.1016/0169-8095(94)90006-X

Randall, D., Khairoutdinov, M., Arakawa, A., & Grabowski, W. (2003). Breaking the cloud parameterization deadlock. *Bulletin of the American Meteorological Society*, *84*(11), 1547–1564. https://doi.org/10.1175/BAMS-84-11-1547

Rasch, P. J., & Kristjánsson, J. E. (1998). A comparison of the CCM3 model climate using diagnosed and predicted condensate parameterizations. *Journal of Climate*, *11*(7), 1587–1614. https://doi.org/10.1175/1520-0442(1998)011<1587:ACOTCM>2.0.CO;2

Richter, J. H., & Rasch, P. J. (2008). Effects of convective momentum transport on the atmospheric circulation in the Community Atmosphere Model, Version 3. *Journal of Climate*, *21*(7), 1487–1499. https://doi.org/10.1175/2007JCLI1789.1

Rosa, D., & Collins, W. D. (2013). A case study of subdaily simulated and observed continental convective precipitation: CMIP5 and multiscale global climate models comparison. *Geophysical Research Letters*, *40*, 5999–6003. https://doi.org/10.1002/2013GL057987

Shutts, G. J., & Palmer, T. N. (2007). Convective forcing fluctuations in a cloud-resolving model: Relevance to the stochastic parameterization problem. *Journal of Climate*, *20*(2), 187–202. https://doi.org/10.1175/JCLI3954.1

Sivakumar, B. (2001). Rainfall dynamics at different temporal scales: A chaotic perspective. *Hydrology and Earth System Sciences*, *5*(4), 645–652. https://doi.org/10.5194/hess-5-645-2001

Sivakumar, B. (2004). Chaos theory in geophysics: Past, present and future. *Chaos, Solitons & Fractals*, *19*(2), 441–462. https://doi.org/10.1016/S0960-0779(03)00055-9

Slingo, J. M., Inness, P. M., & Sperber, K. R. (2005). Modeling. In W. K. Lau, & D. E. Waliser (Eds.), *Intraseasonal variability in the atmosphere-ocean climate system* (pp. 361–388): Chichester, UK: Springer Praxis Books.

Slingo, J. M., Sperber, K. R., Boyle, J. S., Ceron, J. P., Dix, M., Dugas, B., et al. (1996). Intraseasonal oscillations in 15 atmospheric general circulation models: Results from an AMIP diagnostic subproject. *Climate Dynamics*, *12*(5), 325–357. https://doi.org/10.1007/BF00231106

Smith, A. B., & Katz, R. W. (2013). US billion-dollar weather and climate disasters: Data sources, trends, accuracy and biases. *Natural Hazards*, *67*(2), 387–410. https://doi.org/10.1007/s11069-013-0566-5

Stevens, B., & Bony, S. (2013). What are climate models missing? *Science*, *340*(6136), 1053–1054. https://doi.org/10.1126/science.1237554

Strømmen, K., Christensen, H. M., Berner, J., & Palmer, T. N. (2018). The impact of stochastic parametrisations on the representation of the Asian summer monsoon. *Climate Dynamics*, *50*(5), 2269–2282. https://doi.org/10.1007/s00382-017-3749-z

Subramanian, A. C., & Palmer, T. N (2017). Ensemble superparameterization versus stochastic parameterization: A comparison of model uncertainty representation in tropical weather prediction. *Journal of Advances in Modeling Earth Systems*, *9*, 1231–1250. https://doi.org/10.1002/2016MS000857

Sundqvist, H. (1988). Parameterization of condensation and associated clouds in models for weather prediction and general circulation simulation, *Physically-based modelling and simulation of climate and climatic change: Part 1* (pp. 433–461). Dordrecht: Springer Netherlands. https://doi.org/10.1007/978-94-009-3041-4_10

Takens, F. (1981). Detecting strange attractors in turbulence. In D. Rand, & L. S. Young (Eds.), *Dynamical Systems and Turbulence, Warwick 1980*. Lecture Notes in Mathematics (Vol. 898, pp. 366–381). Berlin, Heidelberg: Springer.

Toth, Z., & Kalnay, E. (1993). Ensemble forecasting at NMC: The generation of perturbations. *Bulletin of the American Meteorological Society*, *74*(12), 2317–2330. https://doi.org/10.1175/1520-0477(1993)074<2317:EFANTG>2.0.CO;2

Toth, Z., & Kalnay, E. (1997). Ensemble forecasting at NCEP and the breeding method. *Monthly Weather Review*, *125*(12), 3297–3319. https://doi.org/10.1175/1520-0493(1997)125<3297:EFANAT>2.0.CO;2

Tracton, M. S., & Kalnay, E. (1993). Operational ensemble prediction at the National Meteorological Center: Practical aspects. *Weather and Forecasting*, *8*(3), 379–398. https://doi.org/10.1175/1520-0434(1993)008<0379:OEPATN>2.0.CO;2

Waliser, D., Sperber, K., Hendon, H., Kim, D., Maloney, E., Wheeler, M., et al. (2009). MJO simulation diagnostics. *Journal of Climate*, *22*(11), 3006–3030. https://doi.org/10.1175/2008JCLI2731.1

Walser, A., Lüthi, D., & Schär, C. (2004). Predictability of precipitation in a cloud-resolving model. *Monthly Weather Review*, *132*(2), 560–577. https://doi.org/10.1175/1520-0493(2004)132<0560:POPIAC>2.0.CO;2

Wang, W., Kumar, A., Fu, J. X., & Hung, M.-P. (2015). What is the role of the sea surface temperature uncertainty in the prediction of tropical convection associated with the MJO? *Monthly Weather Review*, *143*(8), 3156–3175. https://doi.org/10.1175/MWR-D-14-00385.1

Watson, P. A. G., Berner, J., Corti, S., Davini, P., von Hardenberg, J., Sanchez, C., et al. (2017). The impact of stochastic physics on tropical rainfall variability in global climate models on daily to weekly time scales. *Journal of Geophysical Research: Atmospheres*, *122*, 5738–5762. https://doi.org/10.1002/2016JD026386

Watson, P. A. G., Christensen, H. M., & Palmer, T. N. (2014). Does the ECMWF IFS convection parameterization with stochastic physics correctly reproduce relationships between convection and the large-scale state? *Journal of the Atmospheric Sciences*, *72*(1), 236–242. https://doi.org/10.1175/JAS-D-14-0252.1

Wheeler, M. C., & Hendon, H. H. (2004). An all-season real-time multivariate MJO index: Development of an index for monitoring and prediction. *Monthly Weather Review*, *132*(8), 1917–1932. https://doi.org/10.1175/1520-0493(2004)132<1917:AARMMI>2.0.CO;2

Wheeler, M., & Kiladis, G. N. (1999). Convectively coupled equatorial waves: Analysis of clouds and temperature in the wavenumber-frequency domain. *Journal of the Atmospheric Sciences*, *56*(3), 374–399. https://doi.org/10.1175/1520-0469(1999)056<0374:CCEWAO>2.0.CO;2

Xu, K.-M., Arakawa, A., & Krueger, S. K. (1992). The macroscopic behavior of cumulus ensembles simulated by a cumulus ensemble model. *Journal of the Atmospheric Sciences*, *49*(24), 2402–2420. https://doi.org/10.1175/1520-0469(1992)049<2402:TMBOCE>2.0.CO;2

Xu, K.-M., & Randall, D. A. (1998). Influence of large-scale advective cooling and moistening effects on the quasi-equilibrium behavior of explicitly simulated cumulus ensembles. *Journal of the Atmospheric Sciences*, *55*(5), 896–909. https://doi.org/10.1175/1520-0469(1998)055<0896:IOLSAC>2.0.CO;2

Zeng, X., Pielke, R. A., & Eykholt, R. (1992). Estimating the fractal dimension and the predictability of the atmosphere. *Journal of the Atmospheric Sciences*, *49*(8), 649–659. https://doi.org/10.1175/1520-0469(1992)049<0649:ETFDAT>2.0.CO;2

Zhang, G. J. (2002). Convective quasi-equilibrium in midlatitude continental environment and its effect on convective parameterization. *Journal of Geophysical Research*, *107*(D14), 4220. https://doi.org/10.1029/2001JD001005

Zhang, M., Lin, W., Bretherton, C. S., Hack, J. J., & Rasch, P. J. (2003). A modified formulation of fractional stratiform condensation rate in the NCAR Community Atmospheric Model (CAM2). *Journal of Geophysical Research*, *108*(D1), 4035. https://doi.org/10.1029/2002JD002523

Zhang, G. J., & McFarlane, N. A. (1995). Sensitivity of climate simulations to the parameterization of cumulus convection in the Canadian climate centre general circulation model. *Atmosphere-Ocean*, *33*, 3407–446. https://doi.org/10.1080/07055900.1995.9649539